Preparation of hybrid Molybdenum Disulfide/Single Wall Carbon Nanotubes-n-type Silicon Solar Cells

Thesis submitted to the School of Chemical and Physical Sciences,

Faculty of Science and Engineering, Flinders University

In fulfilment of the requirements for the degree of Master of nanotechnology

November 2017

Shaykha Alzahly

Supervised by:

Prof. Joe Shapter

Declaration

I certify that this thesis does not incorporate without acknowledgment any material previously submitted for a degree or diploma in any university; and that to the best of my knowledge and belief it does not contain any material previously published or written by another person except where due reference is made in the text.

8 November 2017

Abstract

Molybdenum disulfide (MoS_2) is one of the most studied and widely applied nanomaterials from the layered transition-metal dichalcogenides semiconductor family (LTMD). MoS_2 is a two-dimensional material that has a layered structure such as hexagonal an intermediate layer for sulfur (S) and molybdenum (Mo), respectively. MoS_2 has large carrier diffusion length and has a high charge carrier mobility. The nature of band gap of MoS_2 changes from indirect to direct with the reduction in the material thickness from multilayer to few layer to monolayer. Combining SWCNTs and MoS_2 will provide novel photovoltaic devices. The most common method for the synthesis MoS_2 is exfoliation that that used in this experiment. In this report, MoS_2 is added to SWCNTs-n-type-Si solar cells. Then the films were examined using Scanning Electron Microscopy (SEM), Atomic Force Microscopy (AFM), and Raman spectroscopy. The MoS_2 flake's thickness was from 5-90 nm while the nanosheet's lateral dimensions size range up to 1 μm^2. From Raman spectrum, the MoS_2 peaks appeared at ~384 cm^{-1} and ~408 cm^{-1} that are assigned to E^1_{2g}, and A_{1g} vibrations modes, respectively. This insertion of MoS_2 improved SWCNTs-n-type-Si solar cells efficiencies by 5%.

Acknowledgements

I would like to express my sincere gratitude to the people who were supporting, guiding and providing expertise to me during this project. To begin with, I would like to take this opportunity to thank Professor Joe Shapter, for firstly accepting me to be a member of his group. Joe is the main head behind the success of this project. He was always supporting me, happy to answer any questions I had and coming with novel ideas that can develop the project. Besides my supervisor, deepest thanks to PhD candidate LePing Yu and Tom Grace for the training on the solar cells fabrication, the four-Point Probe training and the Solar Simulator.

I would also like to thank Joe's group members; Dr. Cameron, PhD candidate Munkhbayar Batmunkh, PhD candidate Laim Brownlie and Susanne Sahlos, for their great conversations and interesting time and for their useful advice, suggestions, answering my questions, helping in the lab, providing the laboratory's resources. Similarly, Dr. Mahnaz Dadkhah Jazi for training me photolithography for doing the new mask solar cells. Likewise, Dr. David Vincent for both the training on doing HF etching.

I would like to thank Dr. Jason Gascooke, for his assistance with the SEM and Raman training, characterisation and consultation process. In addition, I would like to thank Dr. Christopher Gibson and Alex Sibley for their assistance and support in training and providing AFM images, and the time that they gave me to explain and training me every detail in this instrument was invaluable. Moreover, I want to thank Dr. Cameron Shearer and Dr. Christopher Gibson for providing Raman spectra and AFM images for some required samples.

Great thanks to Flinders University for providing the students with the best studying environment which is best represented by students learning centre and the Hub Plaza for 24 hour services. In addition, I would like to thank CAPS from the dean to the staff for their help. Additionally, the Australian Microscopy and Microanalysis Research Facility (AMMRF) deserves my thanks for the instruments. Finally, my great thanks, appreciation and gratitude to my family for their continuous help and support in particular my mother Fatimah for coming and supporting me during my studies in Adelaide SA, 2017. Last but not the last, I would like to express my deep thanks to King Abdullah Scholarship program for providing the financial support and giving me this golden opportunity to do my Masters degree of Nanotechnology and to Flinders University students.

Table of contents

List of figures

List of tables

Glossary of abbreviations

Abbreviation	Definition
1D	one dimensional
2D	two dimensional
Ω	frequency of phonon
%T	percent transmittance
AFM	atomic force microscopy
BOE	buffered oxide etch
CNT	carbon nanotube
CNT-Si	carbon nanotube-Silicon
CO_2	carbon dioxide
D-band	disorder Band
eGaIn	eutectic gallium indium
FF	fill factor
HF	hydrofluoric acid
HCI	hydeogen chloride
J_{SC}	short circuit current density
J-V	current density-voltage
MCE	cellulose ester membrace
n-Si	n-type silicon
PCE	power conversion efficiency
PV	photovoltaics
RBM	radial breathing mode
SEM	scanning electron microscopy
Si	silicon
SiO_2	silicon oxide
SWCNT	single-walled carbon nanotube
TMDCs	transition metal dichalcogenides
UV-Vis	ultraviolet-visible spectroscopy
V_{OC}	open circuit voltage

Chapter 1: Introduction

1.1 Overview

Global energy demand has increased dramatically in recent years due to the rapid increase in world population, use of modern technologies, and improved standards of living. According to the U.S Energy department, by 2050, the global energy demand will double, and by 2100, it will be triple the current demand [1]. Burning of fossil fuels continues to account for most of the world's energy production of 16.4 Tw [2]. It is known that burning of fossil fuel causes environmental pollution, which is one of the biggest environmental challenges facing the world today. Fossil fuels used in energy production include natural gas, coal and oil. The use of these fossil fuels result in the emission of CO_2, a greenhouse gas that has largely contributed to the problem of global warming and climate change [3]. According to United States Environmental Protection Agency, CO_2 contributes 65% of global greenhouse gas emissions, with 25% of these produced in electricity and heat production. This has a huge potential to cause serious environmental problems if quick measures are not taken [4].

As a measure to protect the environment and meet the current energy demand, alternative sources of energy have to be considered. This includes development of wind power [5], fuel cells [6], biofuels [7], and solar cell technologies [8]. These alternative energy technologies have the capability to meet the world's energy demand if well developed. However, the challenge is that these resources are small in relation to the required energy supply and are geographically limited to areas the resource is in abundance and consistent. Thus, these four alternative sources of energy can only supplement the world energy requirement, but not fully meet the demand[9]. It is only solar energy that can be harnessed almost everywhere in the world, providing a possible solution to the current energy demand [9]. Solar thermal technologies can be used to capture the sun's heat energy and release it to provide base load power. Roof top solar arrays with black tubing for heating domestic water is a simple technology of base power load from the sun's heat energy. Large-scale thermal farms cannot convert thermal energy into electrical energy using a steam turbine, even though they have a medium to store the energy. In addition, there is also the requirement for steady supply of water [10]. There are many next solar photovoltaics of next generation including the CNT-Si heterojunction.

1.2 CNT-Si solar cells

Since nanotube-silicon heterojunction solar cells were reported by Wei et al. in 2007, they have been widely studied because of their potential to replace the crystalline silicon solar panels that are in use today [11]. Carbon nanotube-silicon heterojunction (CNT-Si) solar cells possess a high solar-to-electricity conversion efficiency and can be manufactured using simple, inexpensive materials using an easy fabrication procedure. Studies have reported 15% efficiency when the CNT is doped with H_2O_2 and HNO_3, and using TiO_2 as an antireflection layer [12]. These findings present solid evidence that CNT-Si devices will possibly replace silicon solar cells [13]. Typically, the CNT-Si cell is similar to the conventional n-type silicon cell, but in CNT-Si devices, a highly transparent film of CNT replaces the p-type silicon layer and the front metallization. Silicon absorbs photon energy from the incident light, creating electron-hole pairs that move to the depletion region where separation occurs under the influence of in-built potential due to equilibration of Fermi-level across the CNT-Si heterojunction [14]. After separation of electrons and holes, they act as the majority charge carriers in Si substrate and CNT film respectively, as shown in **Figure1**. CNT-Si cells are potentially cheap, semi-transparent, flexible, have excellent conductivity, and efficient even under low light [15].

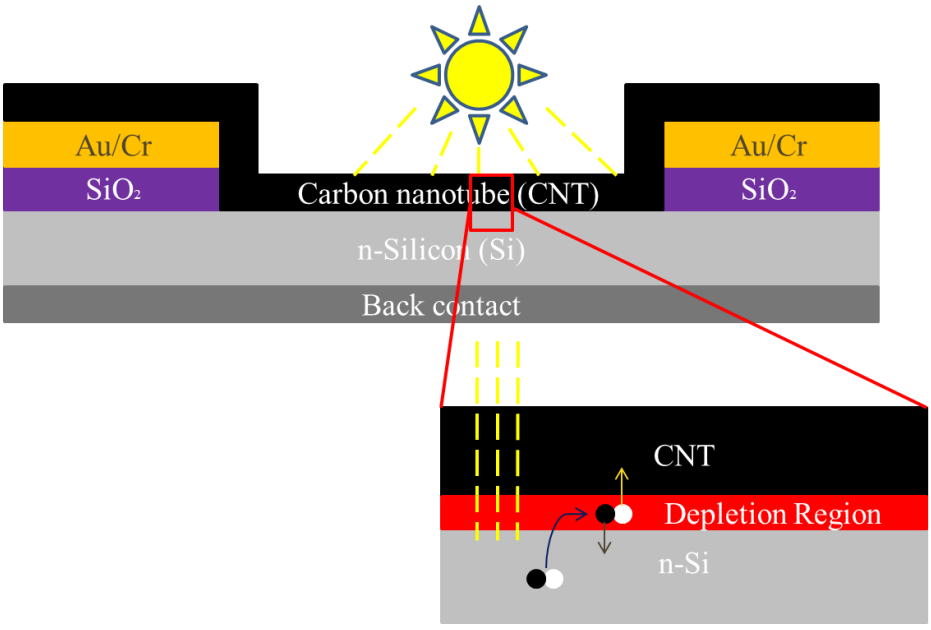

Figure 1: *How CNT-Si solar cells work, (LePing Yu, private communication)* [16].

The first reports of carbon nanotubes (CNTs) and single walled carbon nanotubes (SWCNTs) first emerged in early 1990s. Since then, research in the field of carbon nanotubes

has continued to increase, making it arguably the best-known nanomaterial in the field of nanotechnology. This is because of the excellent electrical and optical properties that are exhibited by this nanomaterial [17] CNTs are allotropes of carbon in which the atoms of carbon form a hexagonal sheet which is seamlessly rolled up to form a cylindrical structure a few nanometers in diameter and microns long. It is the hexagonal shape formed when the C-C atoms bond to each that leads to some unique properties that can find use in many applications [18]. Single walled carbon nanotubes develop p-type characteristics when they exposed to atmosphere due to the adsorption of oxygen molecules. Also the CNTs transport charge carriers with little resistance [2].

However, several important issues remain to be fixed for more development of the CNT-Si-solar cells performance and to enable the change from the basic study to the development of technological applications. A high Schottky barrier at the interface of the Si substrate and the CNTs controls the efficiency in CNT based solar cells devices. Improvement of the Schottky barrier via using an effective carrier transfer layer should able the transport of a high current without any loss of carrier recombination [19] .

It is known that the semiconducting 2H phase restricts the conductivity of MoS_2, which can be overcome via using high conductive CNTs. Additionally; it is found that the SWCNTs have a challenge to hop charge carriers from one tube to another. Two-dimensional material like molybdenum disulfide (MoS_2) can be successfully applied in this case because it will help carriers charge better as it has a long carrier diffusion length (200-500cm^2/Vs) [20]. Therefore, MoS_2 is capable of transporting the holes easily rather than having the charge carriers hopping between the CNTs. The insertion of MoS_2 will decrease the number of hops of charge carrier between the CNTs, which will provided novel photovoltaic devices and enhance efficiency [21]. **Figure 2** is shown how adding MoS_2 to CNTs-Si.

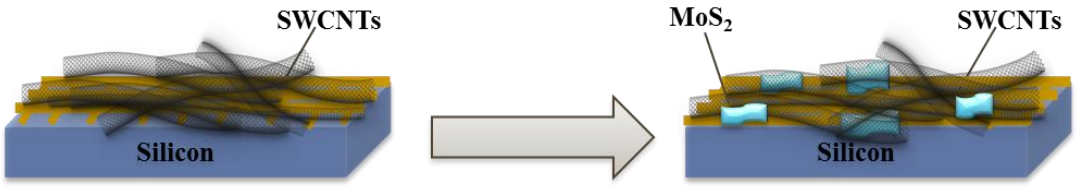

Figure 2: *A schematic of adding MoS2 to CNTs-Si*

1.3 Molybdenum disulfide (MoS_2)

MoS_2 is one of the most studied and widely applied nano electronic transition metal dichalcogenides (TMDs). Like other TMDs, the material in its bulk state is an indirect band gap semiconductor with band gap of 1.2 eV [22, 23]. When the material is formed into a monolayer, the band gap becomes a direct band gap of 1.9 eV [23]. Due to this effect, bulk MoS_2 and its monolayer have been studied extensively [24], with more research conducted on the potential applications of monolayer MoS_2 in 2D devices. The existence of the large gap in the monolayer of MoS_2 has found applications in areas such as field effect transistors with an on/off ratio as high as 10^8 [25], integrated circuits [26], sensors [27] and logic operations [28]. MoS_2 is made of multiple monolayers that are bonded together by weak van der Waals forces. The monolayers consist of S-Mo-S units that are hexagonally packed [29] , **Figure 3**.

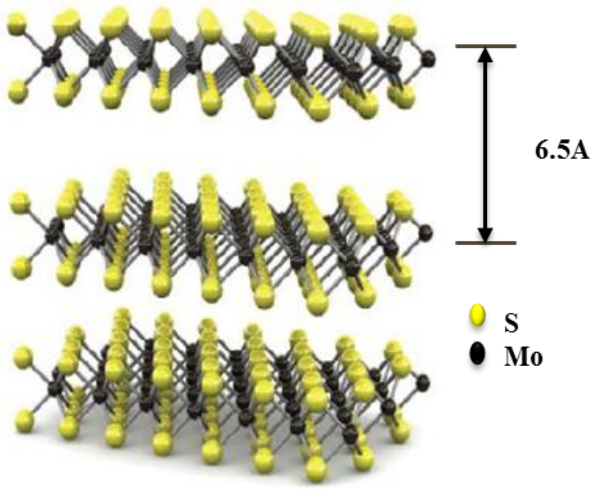

***Figure 3**: Crystal structure of MoS_2 [25].*

The S-Mo-S layers are held in position by different stacking orders resulting in octahedral or trigonal prismatic coordination of the Mo atom, with the unit having a tetragonal, hexagonal or rhombohedral symmetry depending on the orientation of the atoms [30]. The overall 2H structure of MoS_2 exhibits a hexagonal symmetry with the Mo atom having a trigonal prismatic coordination. The naming of 2H is because this phase is made of two layers per unit. To each atom of Mo, six atoms of S are attached. **In Figure 4 (a),** it is shown that the S atoms are positioned below the 3 S atoms bounded on top of the Mo atom in the 2H phase.

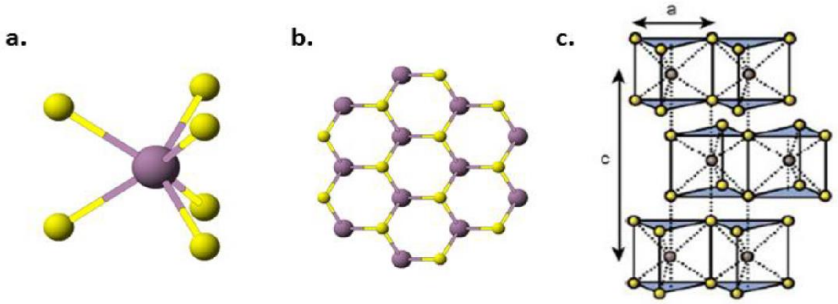

***Figure 4**: MoS_2 2-H structure: a) A single unit of 2H MoS_2 in 3-D model; b) top view of 2H MoS_2 in 2D [31]; c) Three-layer 2H MoS_2 showing 2 layers for every unit hexagonal structure [32].*

With this orientation, only three atoms of S can be seen bonded to Mo atom when the 2H structure is viewed from above **(see Figure 4 (b)).** Since the d orbitals of MoS_2 in the 2H phase are fully occupied, the material behaves like a semiconductor [33].

Figure 5 shows the 1T structure of MoS_2. This structure exhibits tetragonal symmetry with Mo atom having octahedral coordination. The naming of 1T is due to the presence of a single layer per unit in this phase which is analogous to the 2H phase.

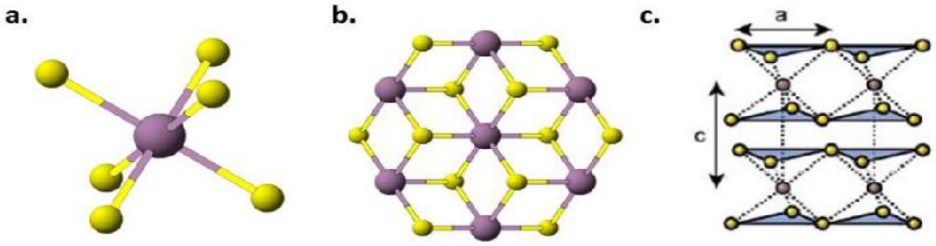

***Figure 5:** MoS_2 1T structure: a) A single unit of 1T MoS_2 in 3D model; b) Top view of 1T MoS_2 in 2D [31]; c) Two layers of 1T MoS_2 showing a single layer per unit tetragonal structure [32].*

The bottom plane of S atoms is rotated by 60^o in relation to atoms on the top plane. For this reason, all the S atoms bonded to Mo atom can be seen when viewed from above. This 1T phase of MoS_2 is metastable and metallic in nature [34] .

There are two methods to produce 2D MoS_2: micromechanical exfoliation and liquid phase exfoliation. Both methods begin with bulk MoS_2 to produce flakes of MoS_2. In micromechanical exfoliation, the flakes are extracted from the bulk by peeling off using sticky tape. Liquid phase exfoliation involves mechanical means such as shearing, grinding,

sonication, stirring, bubbling and grinding [35], or via atomic intercalation through solution chemistry.

MoS_2 exhibits robust mechanical properties. It has good photo-responsivity when used as a monolayer, allowing use in innovative solar cell devices [16]. Inclusion of CNT improves charge transport, thus, when MoS_2 and CNTs are combined, they can provide novel photovoltaic devices with excellent electrochemical performance. The performance of CNT-Si hybrid solar cells also depend on the thickness of the CNT film particularly for films with an average transmittance of >70% [15]. Other research studies done in this field have shown that addition of a conducting polymer, such as polyaniline, into the CNT film enhances electrical conductivity and the therefore, improves the performance of the solar cells [14].

Motivation

With the increasing global energy consumption and the commitment to reduce the amounts of CO_2 and other greenhouse gases emitted into the atmosphere, there is a great need to improve the current photovoltaic systems and develop other sources of renewable energy. There is need to increase the energy conversion efficiency of photovoltaic systems. CNTs and MoS_2 have unique physical properties and ability to use simple solution processes for their deposition and application, thus, these materials present an obvious avenue for increasing PCE and achieving high-energy efficiency compared to current solar panels. In achieving the aim of this research, the following objectives are to be met.

i. Characterise the materials formed using Scanning Electron Microscopy (SEM), Atomic Force Microscopy (AFM), Raman spectroscopy and Ultraviolet-visible (UV-Vis) spectroscopy.

ii. Construct SWCNTs – Si solar cells to be used as reference, as shown in **Figure 6A**, and then adding MoS_2 by:

   a) Designing hybrid MoS_2/SWCNTs films n-type Si solar cells, **Figure 6B**.

   b) Designing SWCNTs @ MoS_2 layered n-type Si solar cells, **Figure 6C**.

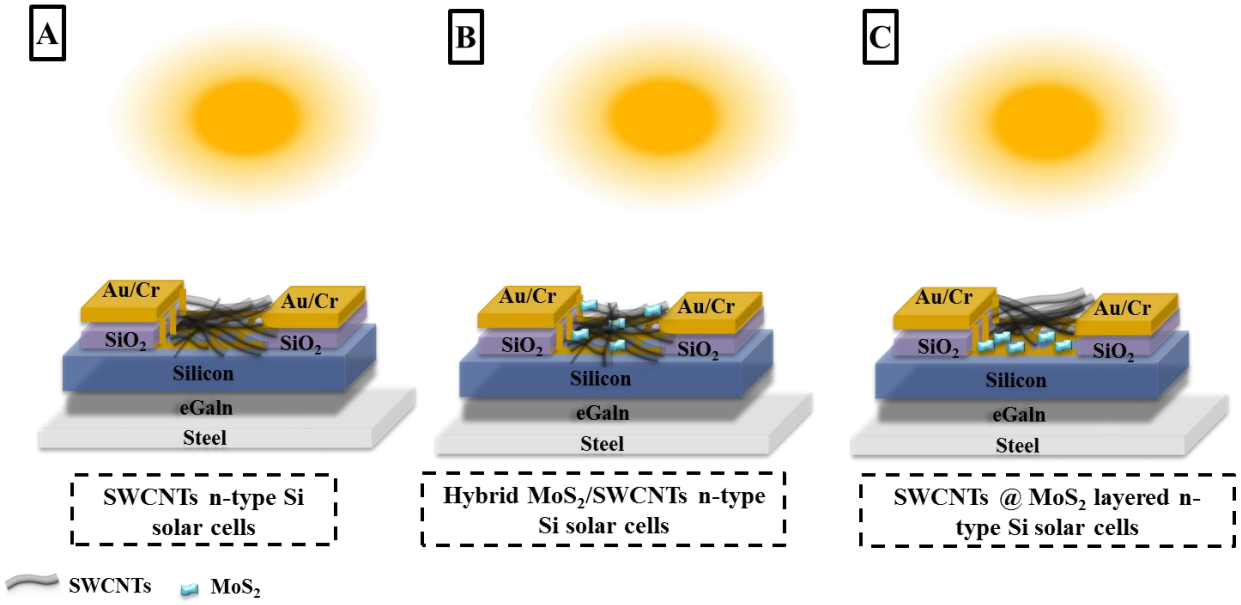

Figure 6: *Schematic structure for, A. SWCNTs–Si solar cells, B. Hybrid MoS_2/SWCNTs n-type Si solar cells, and C. SWCNTs @ MoS_2 layered n-type Si solar cells*

Chapter 2: Experimental details

2.1 Preparation of the dispersions

2.1.1 Single Walled Carbon Nanotube (SWCNTs) dispersion

A single-wall carbon nanotube (SWCNT) stock solution (0.005 g) was prepared by dispersing arc-discharge powder (P3-SWNT, Carbon Solutions Inc., USA) in aqueous Triton X-100 (1% v/v, 50 mL) (Sigma-Aldrich, Australia) by bath sonication (≈50 W_{RMS} (root mean squared Watts), Elmasonic S 30H,) for 3× 1 h intervals at room temperature. The resulting CNT suspension was centrifuged for 1 h, at 17,500g (Beckman Coulter Allegra X-22 Centrifuge (Brea, CA, USA). Then, from all six-centrifuge tubes, the upper two thirds of the supernatants was carefully collected, and then centrifuged again in the similar manner as previously, with the bottom residue being discarded. The upper two thirds of the supernatants from this second centrifuge cycle were then collected and combined to yield the stock solution. The remaining third of unsuspended carbon which contained black lumps was discarded [36], as shown in **Figure 7.**

Figure 7: *As-raw material of SWCNTs is dispersed in solution using sonication and centrifugation [36, 37].*

2.1.2 Molybdenum disulfide (MoS_2) dispersion

Molybdenum disulfide (MoS_2) aqueous dispersion (FlexeGRAPH, Australian National University) was sonicated (S 30H, Elmasonic) for three minutes to make homogeneous suspension. The suspension was diluted with Milli-Q water using a ratio 12.5, 37.5 mL of MoS_2 and water respectively, 25%v/v. Centrifuging (Beckman Coulter Allegra X-22 Centrifuge (Brea, CA, USA) was used at 3000rpm for 10 minutes, whereby afterwards the upper two thirds

of the supernatants from all six centrifuge tubes was collected, combined, and then centrifuged again in the same manner as previously, with the bottom residue being discarded. The upper two thirds of the supernatants from this second centrifuge cycle were then collected and combined to yield the stock solution, with the bottom residue being discarded. The upper two thirds of the supernatants from this second centrifuge cycle were then collected and combined to yield the stock solution, as showing in **Figure 8.**

Figure 8: *As-raw material of MoS_2 is dispersed in solution using sonication and centrifugation.*

2.2 Preparation of Si wafer- Photolithography

An n-type Si wafer doped with phosphorous was rinsed using acetone and dried under a stream of nitrogen. The resistivity of the 525 μm thick wafer was 1-5 Ωm, with 100 nm thermal oxide, (ABC GmbH, Germany). In a clean room, the Au grid structure with an active area of 0.087 cm^2 was defined by photolithography, as shown in **Figure 9**. By using spin coating at 3000 rpm for 30 s a positive photoresist (AZ1518 micro resist technology GmbH, Munich, Germany) was placed on the Si wafer, and then softbaked on a hot plate (AREC heating magnetic stirrer from Rowe Scientific) at 100 ^oC for 50 s. The coated wafer was cooled to room temperature before defining the grid patterns using a mask aligner –EVG 610. The wafer was then inserted in a developer solution – (AZ 726 MIF, obtained from AZ Electronic Materials, GmbH, Munich, Germany) for 15 s to develop photoresist. The wafer was then rinsed with water and dried under a stream of nitrogen gas. The Si wafer post-baking process was done on a hot plate with the pattern defined at 115 ^oC for 50s. Using a Quorumtech, Q300T-D) sputter coater with a quartz crystal microbalance observing the thickness, the metal electrode of gold

and chromium layers (Au/Cr 145/5 nm) was coated on Si wafer. The substrate was then immersed in acetone for about 90 minutes followed by a mild rub in order to dissolve the photoresist. Solar cell substrates were then prepared by cutting pieces of Si sized 1.5 cm^2. One drop of buffered oxide etch (6:1 of 40% NH4F and 49% hydrofluoric acid (HF), Sigma–Aldrich) was applied on the surface and the active area to remove the SiO_2 layer on the surface [38]. To establish the reaction rate, a controlled test was first performed on a piece of Si before applying on the cell substrates.

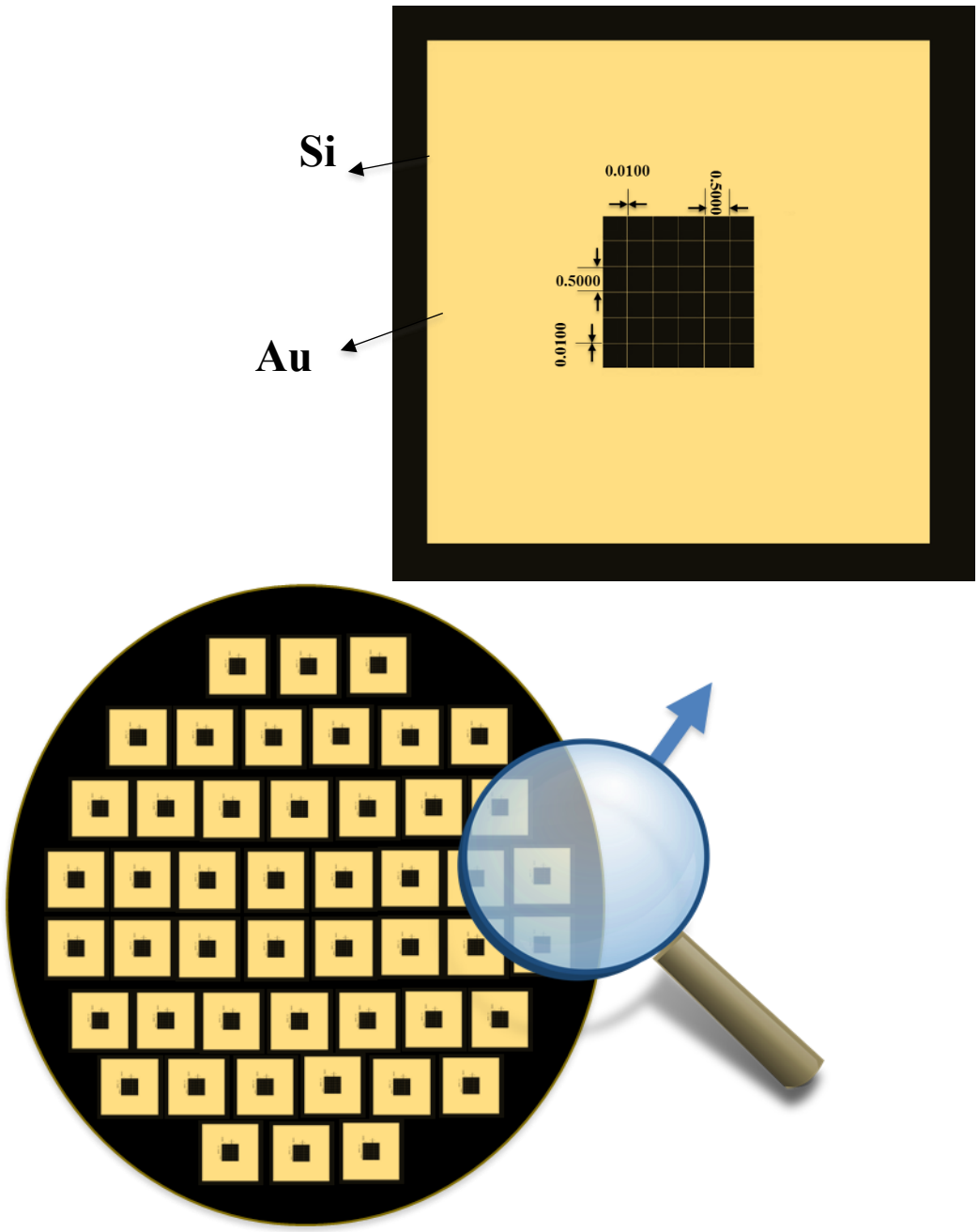

Figure 9: *N-type Si is applied with Au grid structure using photolithography* [39].

2.3 Fabraction of device

2.3.1 SWCNTs-n-Si- solar cells

Nanotube films were prepared using vaccum filtration. This was completed by initially mixing an appropriate amount of CNT suspension (dependent upon the transmittance and the concentration of the suspension) with milliQ water (Kansas City, MO, USA) to make a solution of 250 mL. The suspension was then vaccum filtered with a water aspirator through two types of cellulose ester membrane (MCE). The filter paper on the bottom (VSWP Millipore, 0.025 μm pore size) was patterned with four holes similar to the size of the desired CNTs films. The top filter paper, (HAWP Millipore, 0.45 μm pore size) remained unpatterned. The difference in the rate of flow through the filter papers causes preferential flow of solution through the top film where the bottom film is patterned. Thus, the CNTs are stacked by the top film in a similar shape as that of the template film. After the solution passes through both films, it was passed through the filtration media two more times to allow enough CNTs to be retained on the film. After this, pure Milli-Q water was passed through the CNTs again. The template used in these experiments produces four idential 0.5 cm^2 films in each filtration, (see **Figure 10)**. One film is disposited on a microscope slide for measurement of sheet resistance and optical transmittance, while the others are for attaching to solar cells substrates for measurement of cell efficiency.

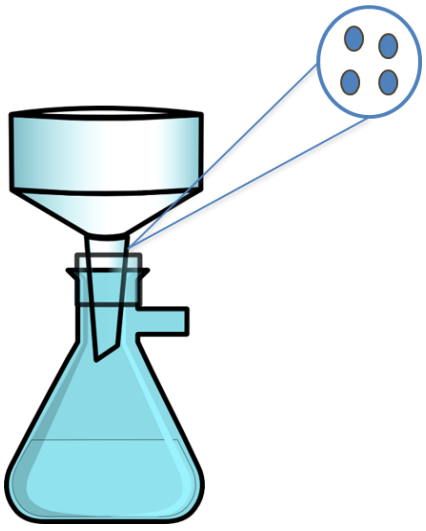

Figure 10: *The template with four holes is used to produce film using vacuum filtration.*

For films depostion, the films were cut from the MCE membrane and placed (CNT side down) on the substrate. Wetting was done using a small drop of water and the nanotube

sandwiched between a piece of Teflon and a piece of glass clamped together. The substrate was then heated at 80 ^{o}C for about 15 minutes, then cooled in darkness for 30 minutes. The substrates were then washed in acetone three times washed for 30 minutes each, second and third wash with stirring to remove the MCE membrane. To complete the preparation of cells, the oxide on the reverse side of all Si pieces was manually removed by scratching to remove the layer of oxide. A gallium indium eutectic (eGaIn) was then applied on the back surface of Si before attaching a piece of stainless steel on the back contact of each piece (**see Figure 11**). The cells were then tested 3 times and further subjected to different post-fabrication treatment procedures. First, a 2% drop of HF was applied on the active area to etch off the SiO_2 formed between the nanotube film and the Si formed during the attachment step of the films. This was then followed by treating the nanotube film with two drops of thionyl chloride ($SOCl_2$) which was left to evaporate to increase conductivity. Before testing, the residue was washed with ethanol and dried under a stream of nitrogen. In the last step, the silicon pieces were treated with 2% HF which significantly improved performance [36]. In addition, The films are disposited on a glass for measurement of sheet resistance and transmittance were also treated but with hydeogen chloride (2%HCI) instead of 2%HF. HF etches glass. Thus, sheet resistance and transmittance was doped 3 times with (2%HCI- $SOCl_2$-2%HCI).

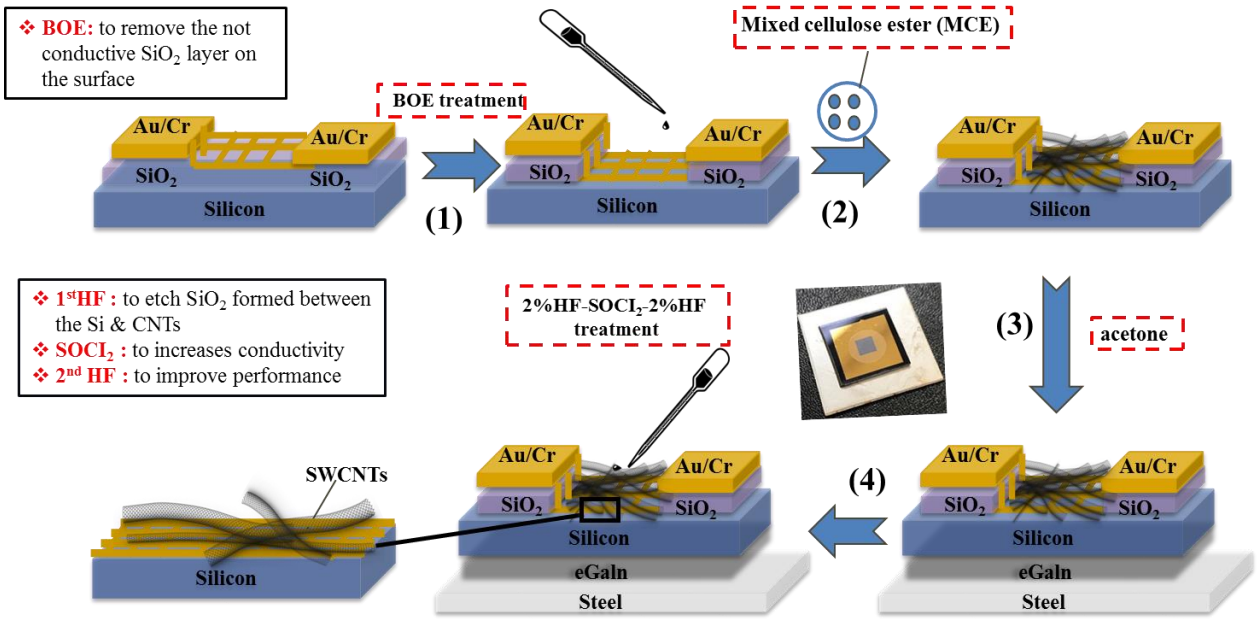

Figure 11: *A schematic of the CNT-n-Si- Solar photovoltaic device fabrication.*

2.3.2 Hybrid MoS_2/SWCNTs-n-Si- solar cells

While keeping the volume of SWCNTs dispersion constant (250 µL) and using a different amount (100-1000 µL) of MoS_2, the dispersions of SWCNT and MoS_2 were sonicated for five mins and 1 h respectively and after mixing, the blended dispersion was sonicated for five mins. Then, the same steps were followed as when making the CNT only cells

2.3.3 Layered MoS_2/SWCNTs-n-Si- solar cells

The dispersion of SWCNTs and MoS_2 were sonicated for five mins and 1 hr respectively. Then, using vacuum filtration, a MoS_2 film using different volumes (100-1000µL) was made while a constant thickness (250 µL) CNT film was also produced. The cells were made by first applying the MoS_2 layer followed by the CNT layer.

2.4 Characterisations of the films

2.4.1 Characterisations the films on glass

A series of (SWCNT, SWCNT with MoS_2 and SWCNT @ MoS_2) films were fabricated from each sample using the SWCNT and MoS_2 solutions and deposited on glass slide (deposited analogously to the previously described film deposition on silicon).

2.4.1.1 Four-point probe (conductivity measurements)

Sheet resistance measurements were completed on SWCNT, SWCNT with MoS_2 and SWCNT @ MoS_2 films using a four-point probe linked to Keithlink software (Solon, OH, USA). Four readings on each film that was on glass at various locations were taken and then results were averaged.

2.4.1.2 UV-Vis spectroscopy (transmittance measurements)

Optical absorption spectroscopy (UV-Vis spectroscopy, (Cary 60)) was performed on the films to determine the thickness as this affects the amount of light passing through the films, and subsequently, the amount of energy produced by the cell. It is important to perform background subtraction using the glass absorbance spectra before calculating transmittance spectra from the absorbance data. The average light transmittance (T) for each sample was determined over a wavelength of 400-850 nm. The %T was calculated according to the equation:

$$\%T = 10^{(2-Abs)} \qquad (1)$$

2.4.2 Characterisation the films on solar cells

2.4.2.1 Solar simulator

At each stage of preparation, the solar cells produced were tested by applying voltage to the electrodes under a solar spectrum simulator illuminating at 100 $mWcm^{-1,}$ and in the absence of natural light. An AM 1.5G filter (obtained from Irvine, CA, USA) was used to filter the light. A silicon reference cell (PV Measurements, from the National Institute of Standards and Technology) was used to maintain irradiance of the sample. A Keithley 2400 SourceMeter (from Solon, OH, USA) was used to acquire data that was captured and sent to a computer with Lab View (Austin, TX, USA).

2.4.2.2 Current density-Voltage (J-V) curves

A current density-voltage characteristic or J-V curve is a relationship between the density of current through a material, and the corresponding potential difference, or voltage [40]. Typically, the relationship is represented as a graph or chart, **Figure 12.** Parameters of J-V curves include:

- **Open circuit voltage (V_{oc})** – This is the voltage where current density is 0.
- **Short circuit current density (J_{sc})** – This corresponds to a short circuit when there is low impedance and the voltage is 0.
- **Maximum power (P_{max})** – P_{max} is the power measured at maximum voltage (V_{max}), and maximum current density (J_{max}).
- **Fill factor (FF)** – This is determined by comparing the maximum power (P_{max}) to the theoretical power (P_T) that is essentially the output at both the V_{oc} and J_{sc} together. It is a measure of the quality of the cell. FF is calculated by:

$$FF = \frac{V_{max} \times J_{max}}{V_{oc} \times J_{sc}} \qquad (2)$$

- **Efficiency (η)** – The conversion efficiency of the solar cell for performance.

$$\eta = \frac{FF \times V_{oc} \times J_{sc}}{P_{in}} \qquad (3)$$

The measurements of the dark current and the light current can be used to determine the cell efficiency. A typical J-V curve showing the above parameters in a solar cell is as below:

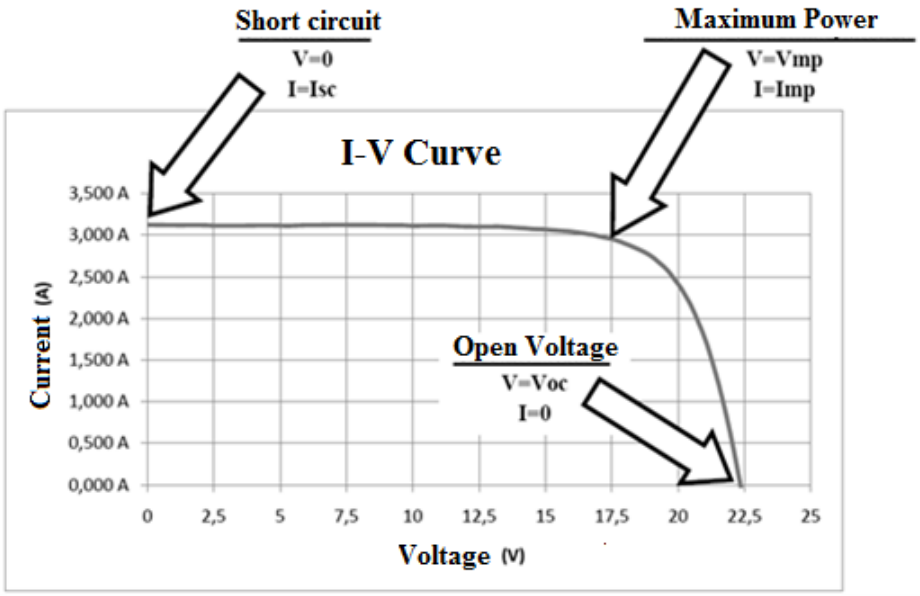

Figure 12: *A J-V curve showing the cell parameters* [41].

2.4.3 Characterisations of the films on silicon

2.4.3.1 Scanning electron microscopy (SEM)

SEM technique was used to characterize the surface structure of the nanostructures after fabrication. The electron beam with a spot size of <5 nm is focused on the solid sample and raster scans the surface. The interactions between the electrons and the surface, electrons are emitted [42]. The emitted electrons are collected on a charge-coupled device detector and used to produce 2D SEM images with information about the external morphology and crystalline structure of the sample, (see **Figure 13**). Contrast changes in the image is as a result of topographical differences and electronic properties on the sample under study[43]. In the current work, we characterised samples using a SEM-FEI-F50 an accelerating voltage range of 10 to 20 kV, and a working distance provided as 10 mm [44].

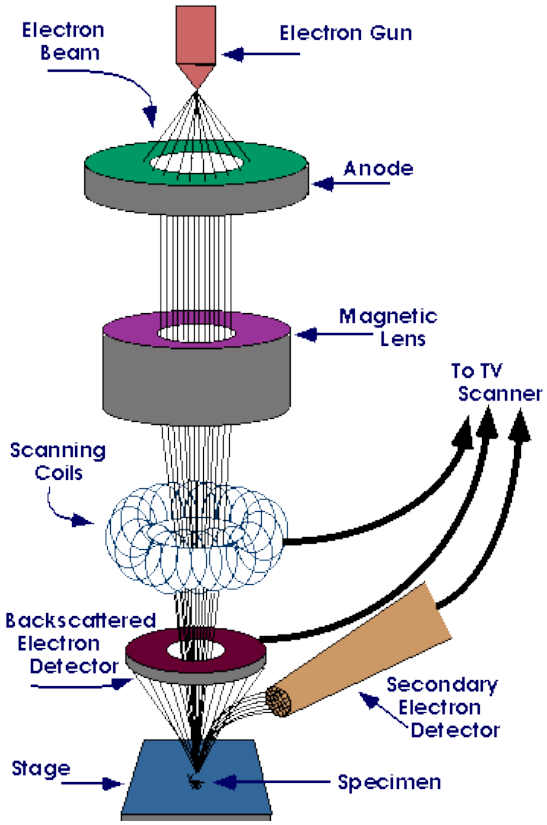

Figure 13: *Schematic showing the salient features Scanning electron microscopy* [44].

2.4.3.2 Atomic force microscopy (AFM)

AFM was used to investigate the topographical structure of the nanostructures formed. This imaging technique was specifically applied for determining the structure of CNTs, pristine flakes of MoS_2, and MoS_2/CNT composites. AFM is an image scanning probe microscopy, which uses a sharp tip fixed on a spring-like cantilever. The tip raster-scans along the x-y grid of a sample surface and the interactions between the probing tip and the sample surface are measured using a reflected laser (see **Figure 14**) [45]**.** There are a number of modes of operating the AFM depending on where it is applied [46] Generally, there are two possible AFM imaging modes: static/contact modes and "tapping"/non-contact modes. In static mode, the tip moves across the sample surface and the surface contours are measured either directly by using cantilever deflections, or using the feedback signal required to maintain a constant cantilever position. In tapping mode, the cantilever oscillates with fixed amplitude along the sample surface. As the sample heights change, so do the interactions between the tip and the sample, resulting in changes in the amplitude of oscillation. A feedback loop continuously adjusts the relative *z* position of the cantilever during the scanning position to maintain a constant oscillation amplitude. The distance moved by the tip is measured to produce a topographical map of the surface [47] .

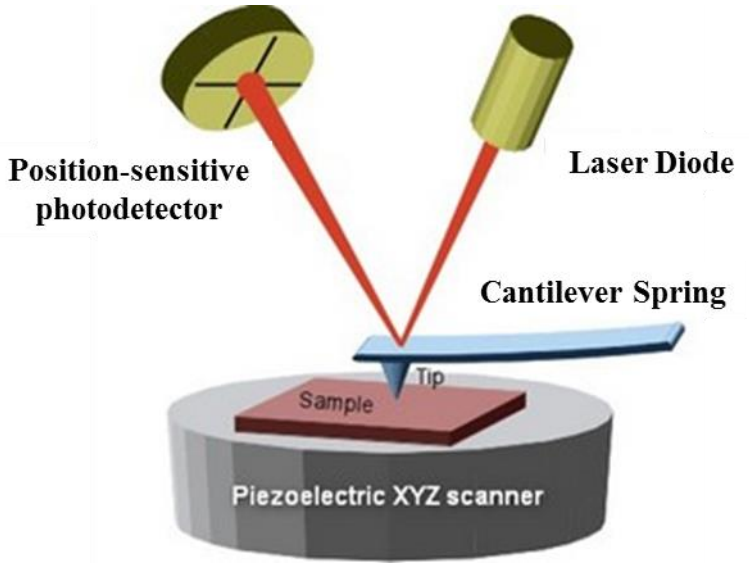

Figure 14: *Schematic showing the salient features Atomic force microscopy (AFM)* [54].

In the current project, we used the AFM tapping mode with a Multimode head and a NanoScope V controller, obtained from Digital Instruments, Veeco, Santa Barbara, to take images of the samples under ambient conditions. The cantilevers used were of Silicon type (NSC15 Micromesh) with a fundamental resonance frequency of 200 – 500 kHz. The sample images were acquired at a scan rate of 1.0 Hz with manually optimized set points, amplitude,

and feedback control that varied from sample to sample. The samples presented in this work were flattened using the NanoScope analysis software.

2.4.3.3 Raman Spectroscopy

Raman spectroscopy is an important spectroscopic technique for observing and characterising materials. Typically, when a sample is illuminated with a laser beam, photons are emitted in an electromagnetic radiation. These photons may have the same energy, or may be shifted to higher or lower energies than the incident photon. A final state with higher energy results in the scattered photon shifting to a lower frequency, known as Stokes shift, while a final state with lower energy results in scattered photon shifting to a higher frequency, known as anti-Stokes shift [48, 49]. The energy shifts provide information about the modes of vibration in a system (see **Figure 15**) [50].

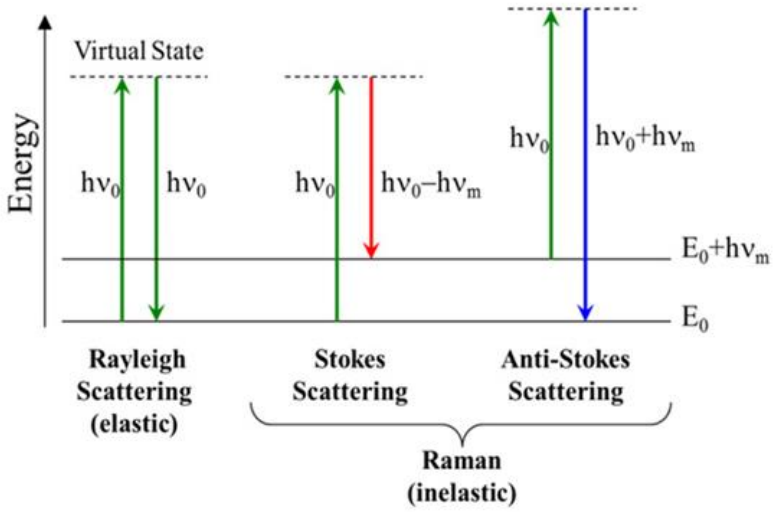

Figure 15: *Possible Raman scattering processes [49].*

CNTs in Raman spectroscopy show characteristic peaks at approximately 1350 cm^{-1} for the D bands, and 1580 cm^{-1} for the G bands. The D band is characterised by disordered carbon species, and on the contrary, the G band is characterized by well-organised carbon species such as CNTs and graphite. A RBM can be observed in Raman spectra of CNTs between 100 and 500 cm^{-1} as an evidence of the presence of SWCNTs in a sample, **Figure 16**. A G' band from a 2-phonon, 2nd order Raman scattering is expected at 2700cm^{-1}[36, 51]. At 1550 cm^{-1}, a signal called a Breit-Wigner-Fano (BWF) band, which is due to metallic carbons, appears in the spectra [52].

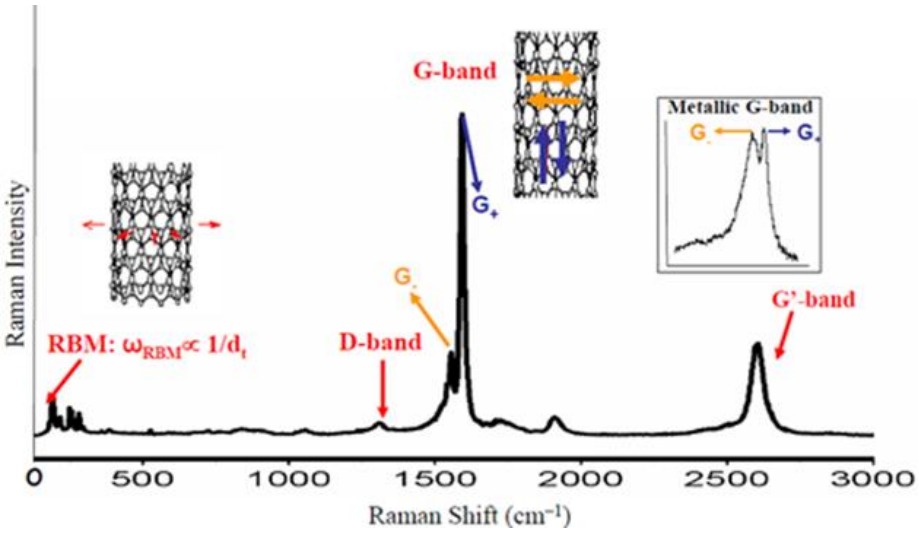

Figure 16: *Raman spectra for SWCNTs* [51].

In MoS_2, Raman spectroscopy, the number of layers in different exfoliated flakes can be revealed. Raman spectra at room temperature for N = bulk, 6, 5, 4, 3, 2 and 1 layers of MoS_2 flakes excited using inelastic light in the 532 nm wavelength are shown in **Figure 17(B). Figure 17(A)** shows the atomic vibrations in the in-planeE^1_{2g}, and the out-of-plane A_{1g} [23]. The number of layers present in the crystal structure of MoS_2 determines the Raman shift of the material phonon modes as shown in **Figure 17(C)** [23].

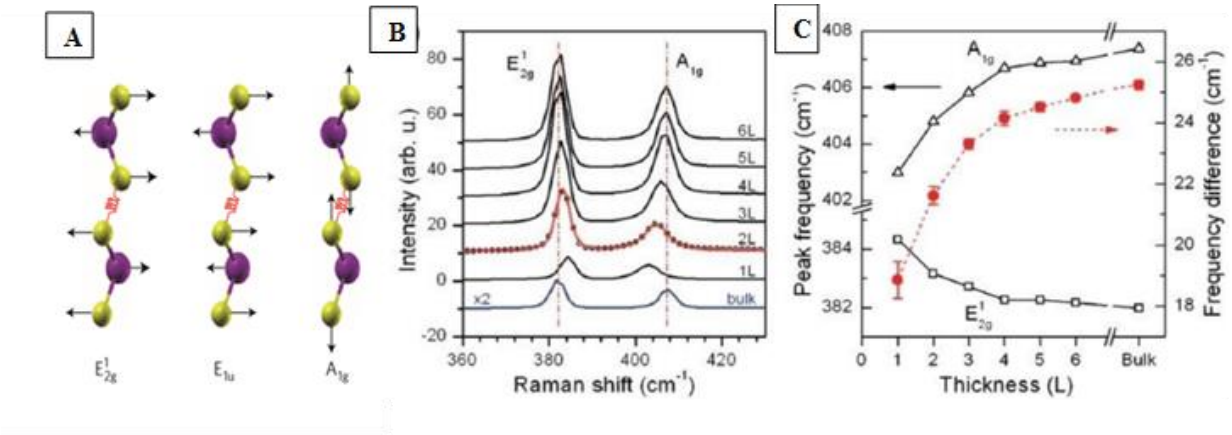

Figure 17: *(A) Raman spectra for MoS_2 with different layers; (B) MoS_2 phonon modes and Raman peak position shifts for $E^1_{2g}$and A_{1g} with different layers; and (C) Frequency difference of the $E^1_{2g}$and A_{1g} modes that can be used to determine the number of layer* [23].

In the current work, Raman spectra was acquired using the Witec alpha300R Raman microscope set at a wavelength of 532 nm, and a 40X objective with a numerical aperture of 0.6. Grating ranged 600 and 1800 g/mm. Integration times for single Raman spectra ranged between 5 s and 60 s for between 1 and 3 accumulations. Confocal Raman images were also

acquired with integration times ranging 10 s per pixel. For each pixel, there is a Raman spectrum. To generate Raman images, the intensity of a given region in the Raman spectrum corresponding to the material is plotted against the *X*-*Y* position of the laser during a surface scan.

Chapter 3: Result and Discussion

3.1 Films characterisations

In order to fabricate solar cells, the films that will be used have to be examined. The films were characterised by using scanning electron microscopy (SEM), atomic force microscopy (AFM), and Raman spectroscopy**.**

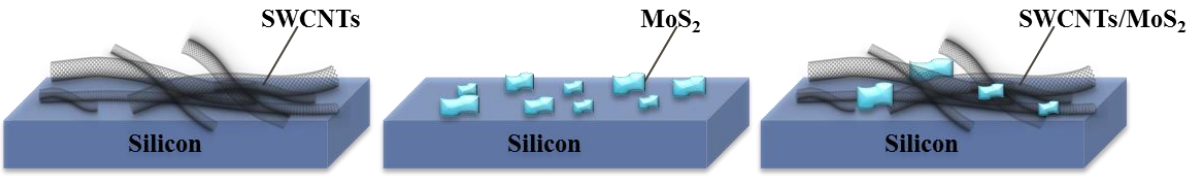

Figure 18: *The deposition of films on Si substrate*

3.1.1 Single Walled Carbon Nanotube (SWCNTs)

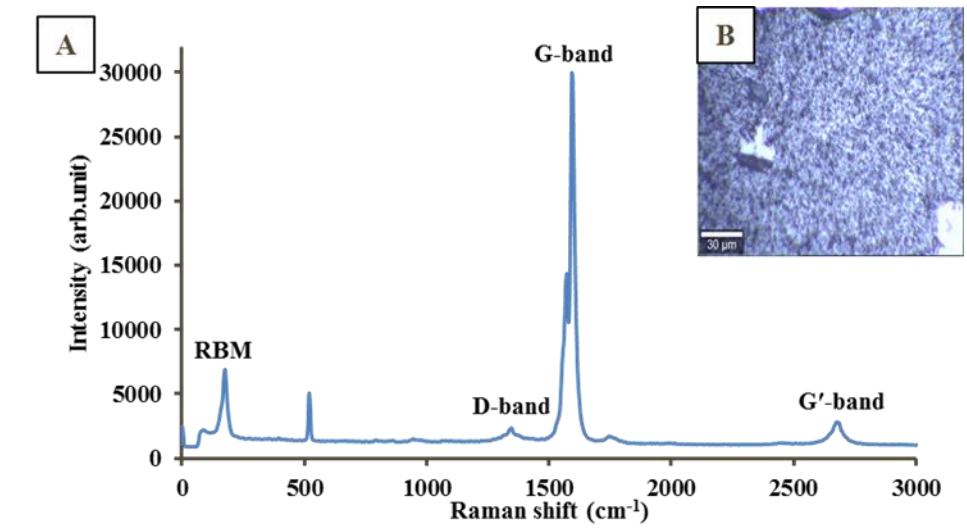

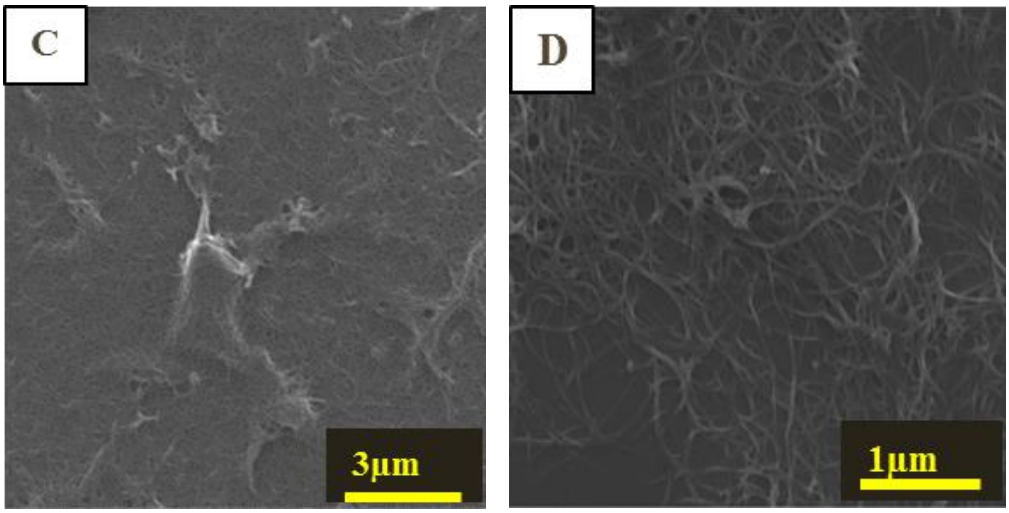

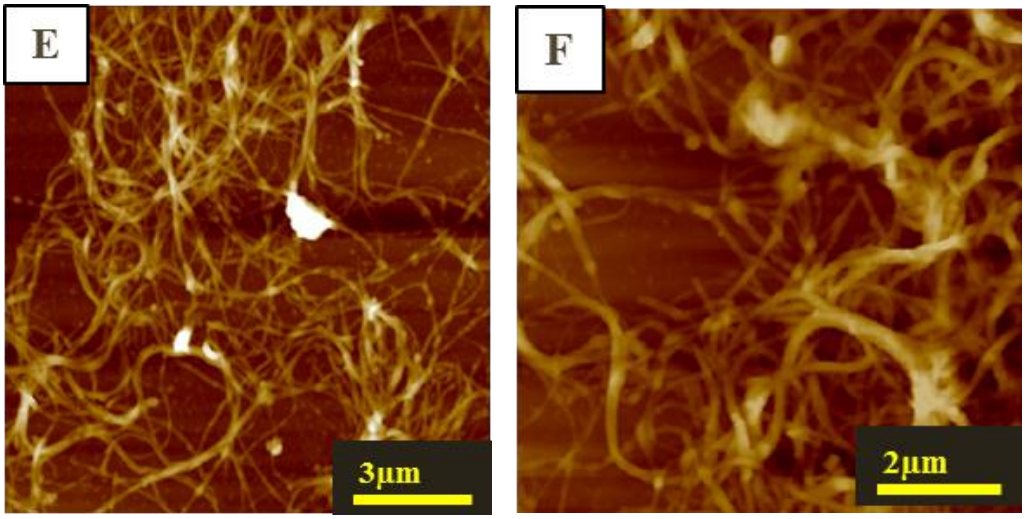

Figure 19: *(A) Raman spectrum and (B) Raman optical image, (C-D) SEM images and (E-F) AFM images of SWCNTs film that deposited on Si substrate.*

Figure 19(A, B) are Raman spectra for SWCNTs and optical imaging were achieved on the Si substrate. **Figure 19(A)** illustrates a Raman spectrum of the SWCNT on Si surface; the peaks monitored in the spectrum are assigned in **Table1**. 521 cm^{-1} is from the silicon substrate. The Raman spectra proved the presence of SWCNTs on the substrate showing the radial breathing mode (RBM). The location of the RBM (ω_{RBM}) provides information about SWCNTs diameter by using the equation (4):

$$\textbf{RBM shift } (cm^{-1}) = A/d_t + B \qquad (4)$$

Where d_t is diameter of the CNT and A, B which are constants which depend on the SWCNTs environment, have previously been measured and the value of A, B are 234 and 10 cm^{-1} respectively. This expression is used with the RBM peak position and was calculated diameter to be 1.4 nm; which is agreement with supplied diameters of the manufacturer [36]. Another common calculation of Raman's SWCNTs is the ratio of the intensities of the D and G- bands (D/G ratio). The (D/G ratio) is often used to calculated the disorder in CNTs samples and the value is ~0.08.

Table 1: *Position of Raman peaks and assignment for SWCNTs on Si.*

Peak Position (cm^{-1})	Acronym	Assignment
176	RBM	radial breathing mode
1350	D-band	disorder band
1593	G-band	graphitic band (axial)
1573	DWF	Breit-Wigner-Fano
2664	G′-band	overtone of D

SWCNT films were deposited on Si substrates and then the film was imaged by scanning electron microscopy (SEM) and atomic force microscopy (AFM) in order to determine the morphology of the films. **Figure 19(C, D) and (E, F)** illustrate SEM and AFM images, respectively. SEM and AFM images show some long cylinders shapes, as expected for SWCNTs. Although difficult to quantify, the length of the SWCNTs average over 1µm, again agreeing with details supplied by the manufacturer. In addition, SEM and AFM show that SWCNTs formed a suspension good enough to make homogenous films on a substrate and are thus utilisable for CNT-Si- solar cell projects and could hybrid with MoS_2.

3.1.2 Molybdenum disulfide (MoS_2)

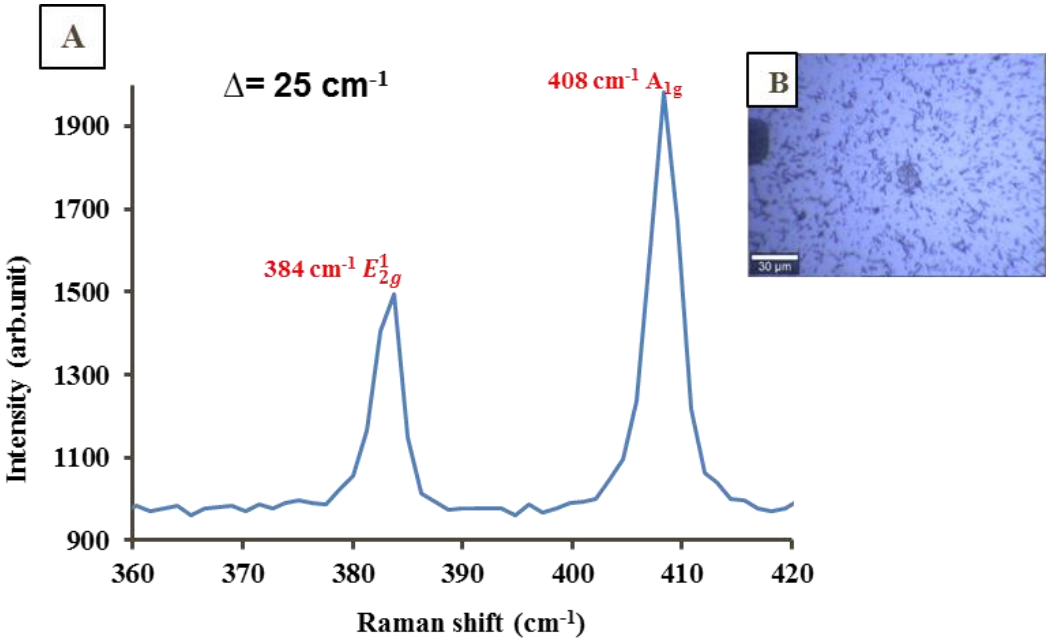

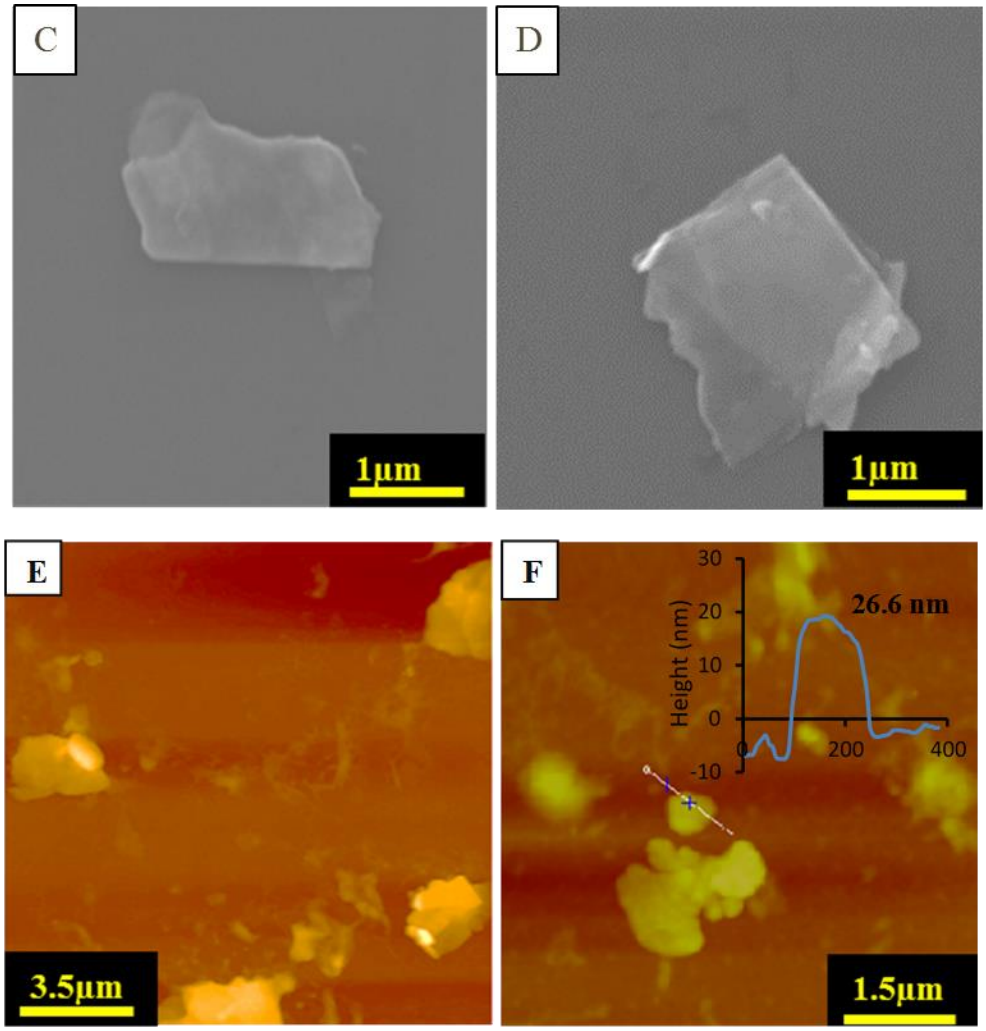

Figure 20: *(A) Raman spectrum, (B) optical image, (C-D) SEM images and (E-F) AFM images of MoS_2 film that deposited on Si substrate and the corresponding line scan of the MoS_2-nanosheet film.*

Raman spectra gives a qualitative characterisation of MoS_2 nanosheets. MoS_2 was deposited on Si substrate and Raman spectra for the exfoliated MoS_2 are shown in **Figure 20A** that expected E^{1}_{2g} peak, at 383 cm^{-1} originates from the Mo−S in-plane vibration mode while, A_{1g} peak is also observed near 408 cm^{-1} from vibrations of out-of-plane. The peak difference between E^{1}_{2g} and A_{1g} was 25 cm^{-1}. That is consistent with the previously studied for values of bulk MoS_2 [23] which the frequency spacing is about 25 cm^{-1} for bulk and 19 cm^{-1} for monolayer [23, 53]. That was expected because AFM provide that the MoS_2 has more than 3 layers.

In **Figure 20(C, D)** and **(E, F)**, SEM and AFM, respectively were used to image substrate. They provide MoS_2 like crystal sheet. SEM is used for determining lateral dimensions of 2D MoS_2 layers. The range of lateral size was 100-1000 nm^2. AFM images give further information on efficient exfoliation of the MoS_2 flaks and the thickness. In order to obtain the thickness of

the nanosheet, cross sections of the AFM images were done to show that the MoS_2 nanosheets have thickness ranging between 5 and 92 nm, each layer has a thickness of ~0.65 nm [23]. The results reveal that the majority of the exfoliated MoS_2 are multilayers. That was expected because the sheets of MoS_2 stacked on each other due to MoS_2 deposed out of dispersion and the solvent disappeared.

3.1.3 Molybdenum disulfide (MoS_2)/ Single Walled Carbon Nanotube (SWCNTs)

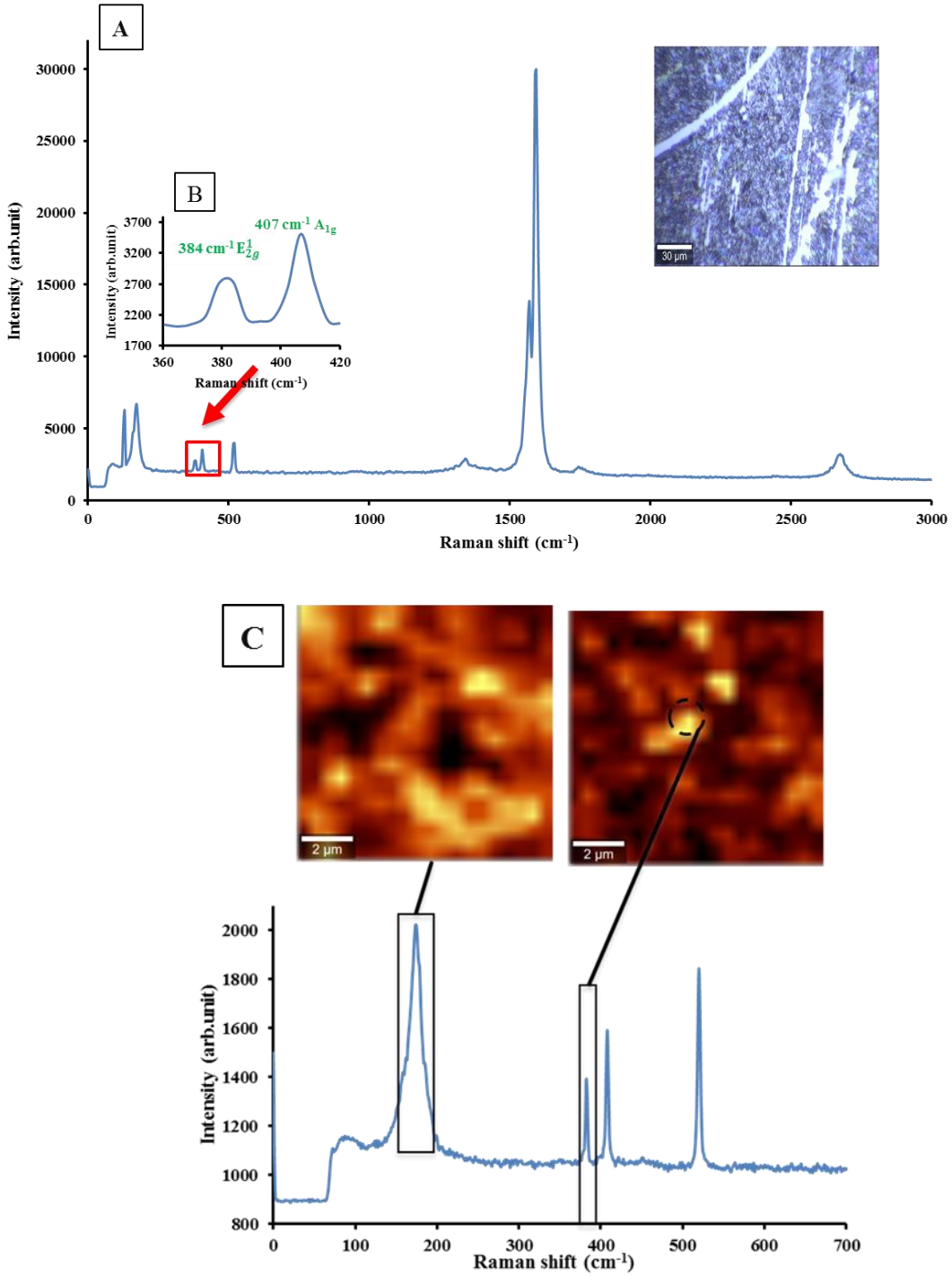

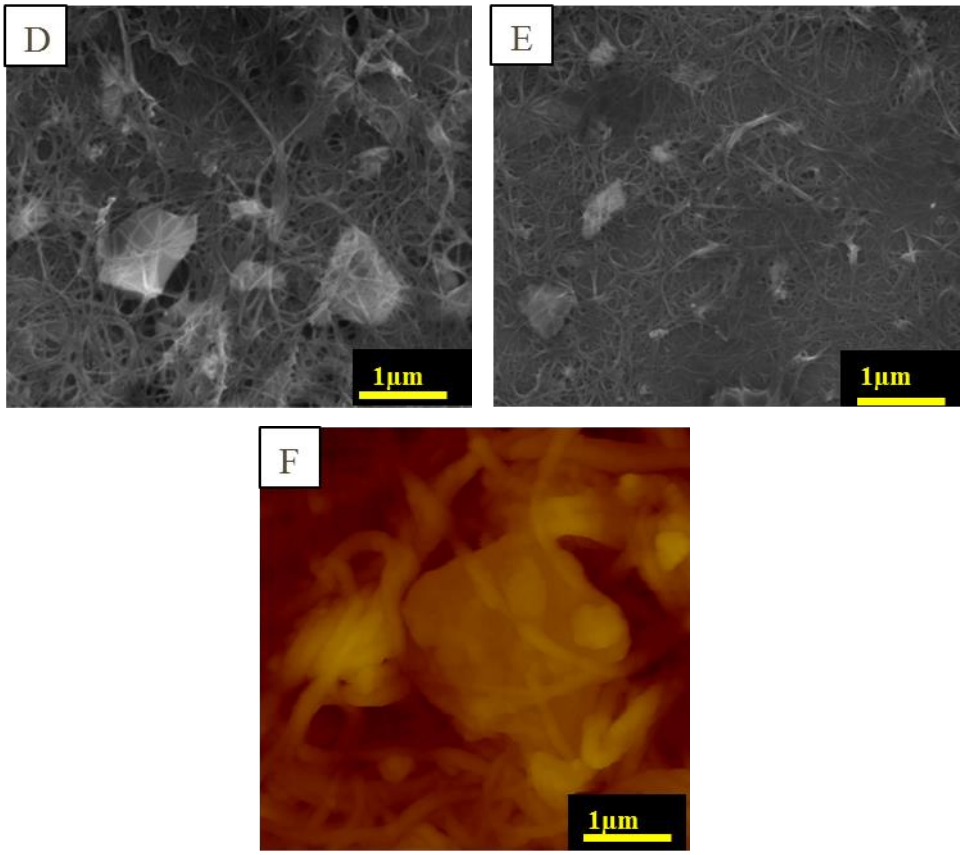

Figure 21: *(A) Raman spectrum with optical microscope image, (B) enlargement of the MoS_2 peaks E^{1}_{2g} and A_{1g} and (C) Another Raman spectral with spectral image, (D-E) SEM images and (F) AFM images of morphological characterization of MoS_2/SWCNT hybrid materials that deposited on Si substrate.*

Figure 21A&B show the Raman spectrum of the hybrid sample, which as expected has the characteristic peaks of both SWCNT and MoS_2. Thus, they can be used to probe the exfoliation of the 2D MoS_2 crystal structure. The E^{1}_{2g} (384 cm^{-1}) and the A_{1g} (407 cm^{-1}) spacing is about 23 cm^{-1}. In addition, the spectra display characteristic of Raman peaks for SWCNTs. Another Raman spectrum was collected and shown the spectral imaging was obtained by integrating the intensity at each (x, y) coordinate and converting the amount for the maximum height of the RBM at around 174 cm^{-1} and the E^{1}_{2g} at around 383 cm^{-1} into a colour, as shown in **Figure 21C.**

SEM and AFM images clearly display the long cylinder shape for SWCNTs and crystal sheet for MoS_2 where the amounts of SWCNTs distributed randomly among the MoS_2 flakes. This proves that SWCNTs/ MoS_2 dispersions are well mixed, as shown in **Figure 21(D,E and F).**

3.2 Characterisation of solar cells

3.2.1 SWCNTs-n-Si- Solar cells and MoS_2-n-Si-Solar Cells

In order to investigate the effect of molybdenum disulfide (MoS_2) on the CNTs-n-Type-Si solar cells, separate SWCNTs and MoS_2 aqueous dispersion were prepared and were used to fabricate n-Si based solar cells (CNT-n-Si and MoS_2-n-Si). This experiment was carried out because it is critical to understand the properties of each material individually for solar cells. One example of those properties that effect the cell performance is the optical transmittance. The transmittance, which depends significantly on the film thickness, is the amount of light that passes through the films. The transmittance of the films decreases with increasing film thickness. The sheet resistivity of the films plays an important role in effectively transporting the charges within the device. The high transmittance is necessary to allow sufficient amount of light to reach the active layer of silicon solar cells. However, the films with high transmittance usually suffer from poor conductivity (high sheet resistivity). There is a clear trade-off between the transmittance and sheet resistivity of the films for solar cells. Therefore, finding an optimum thickness of the transparent and conductive films is of great importance to maximize the PV performance of the fabricated devices. In this project, vacuum filtration was used to prepare the films which is detailed in experimental section. Four measurements on all fabricated solar cells were taken. Briefly, (i) as-prepared solar cells without any pre and post treatments, (ii) first HF treatment to remove the surface attached oxygen groups from the silicon substrate, (iii) $SOCl_2$ doping treatment to increase the conductivity of the SWCNT networks by doping with Cl- atoms; and (iv) lastly, second HF treatment to further remove any oxygen groups that have been introduced during the $SOCl_2$. The results after all these 3 treatments are mainly shown and discussed in the main text of this thesis; and very detailed data after each treatment have been depicted in the Appendix. **Figure22** illustrates the photocurrent-voltage (J-V) characteristics of the best-performing CNTs-n-Si and MoS_2-n-Si solar cells and their detailed photovoltaic performance have been summarised in **Table 2**. It can be seen that SWCNTs based on solar cells have achieved a higher efficiency as compared to the MoS_2 based on solar cells, indicating that the SWCNTs are suitable candidates for this class of solar cells owing to their extremely low resistance as compared to the MoS_2. Moreover, it is well known that MoS_2 is an n-type semiconductor, which will result in no depletion region when n-Si is used.

In order to adjust the thickness of the SWCNT films, the volume of the filtrated solutions was controlled. Lot of previous work in our lab has shown the best transmittance is 75%. A sheet resistivity of 531 **Ω** sq^{-1} is in good agreement with the previously reported value in the literature was obtained [15]. On the basis of that with my dispersion 250 µL is an optimal values and its solar cell exhibited a power conversion efficiency (PCE) of ~ 6.6%. Detailed photovoltaic performances are shown **Table 2.**

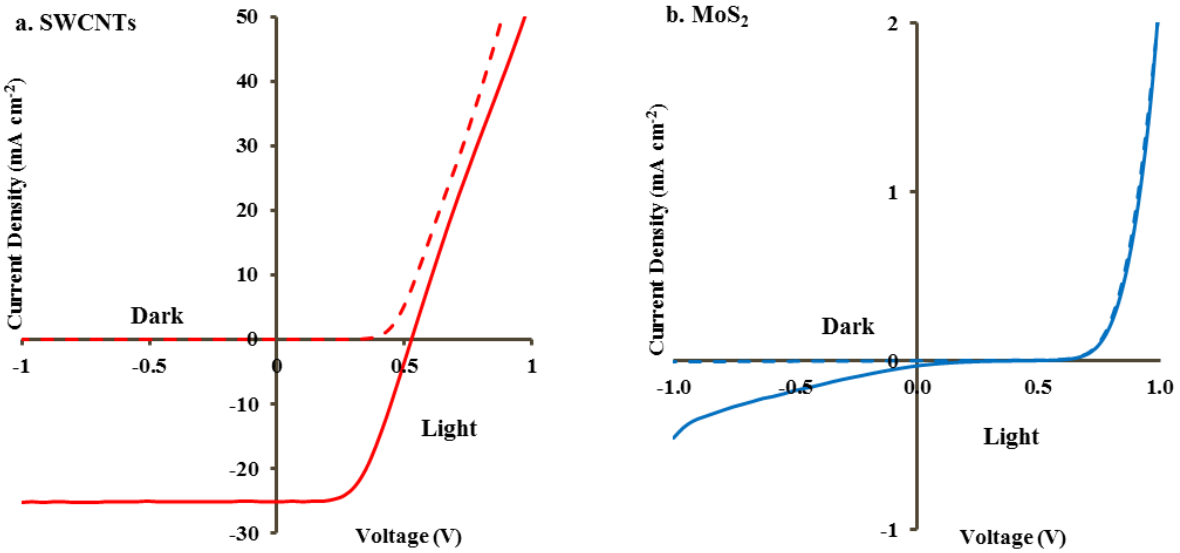

Figure 22: *J-V curves of the best performed (a) SWCNTs-n-Si- Solar cells and (b) MoS_2-n-Si-Solar Cells.*

Table 2: *Solar cell properties for best performing cells for SWCNTs & MoS_2 in bold text, average properties (the errors are estimated by standard deviation from three cells).*

	J_{sc} (mA/cm^{-2})	V_{oc} (V)	T%	R_{sheet} (Ω sq^{-1})	FF	Eff (%)
SWCNT	25.17	0.529	74	531±74	0.53	7.04
	25.4 ±1	0.5±0.01			0.49±0.05	6.6±0.4
MoS_2	0.025	0.236	96	1621±236.6	0.18	0
	0.021±0.004	0.21±0.02			0.2±0.005	0

3.2.2 Hybrid MoS_2/ SWCNTs-Si- Solar cells

After, determining the best volume of the SWCNT suspension was 250 µL, various amounts of MoS_2 dispersion (100-1000µL) were mixed to fabricated 10 different thickness films. **Figure 23** shows adding MoS_2 leads to almost not change in Rsheet. After all treatment of these films, R_{sheet} exhibit values ranging between (512-716 Ω sq^{-1}) compared to SWCNT-only films which gives (531 Ω sq^{-1}). However, the transmittance dropped around 5%.

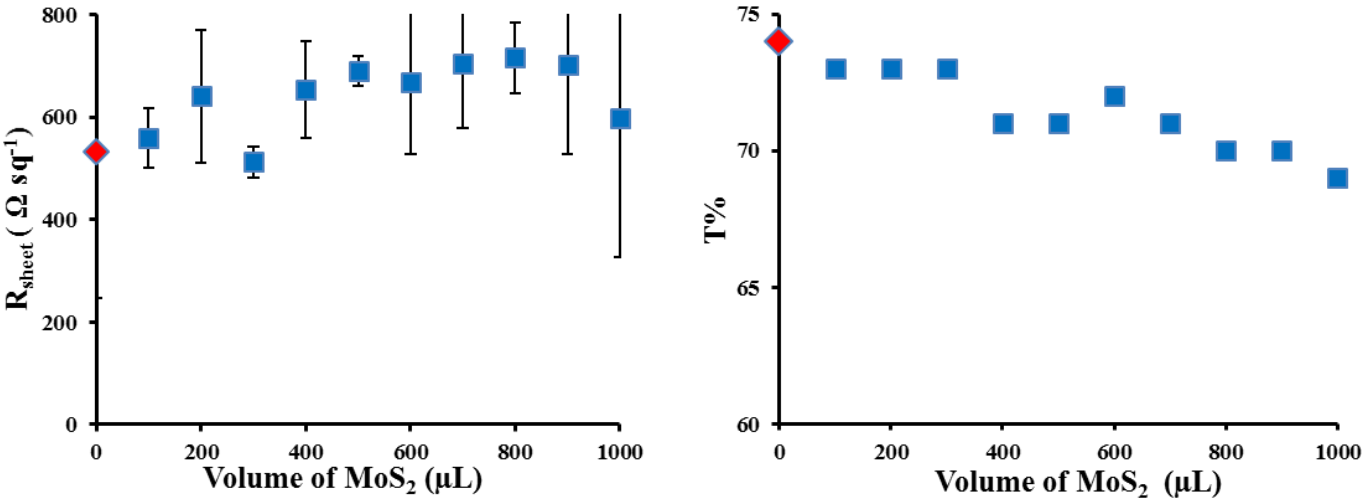

Figure 23: *Sheet resistance and Transmittance of hybrid MoS_2 / SWCNTs films with various thickness after all three chemical treatments.*

Figure 24 exhibits the current- voltage characteristics of the best performing cells for 250 µL SWCNTs-n-Si solar cells and 600µL MoS_2/ 250 µL CNT-n-Si-solar cells after the complete treatment sequence, under the dark and illumination. All samples show similar behaviour under light for the open circuit voltage (V_{oc}), and a slightly a higher short-circuit current density (J_{sc}) for hybrid samples. All photovoltaic parameters of the MoS_2/ SWCNTs/n-Si solar cells are increased in comparison to those of SWCNTs/ n-Si solar cells, which suggest that the MoS_2 hybrid plays an important role in enhancing the photovoltaic performance of solar cells as shown in **Table3**.

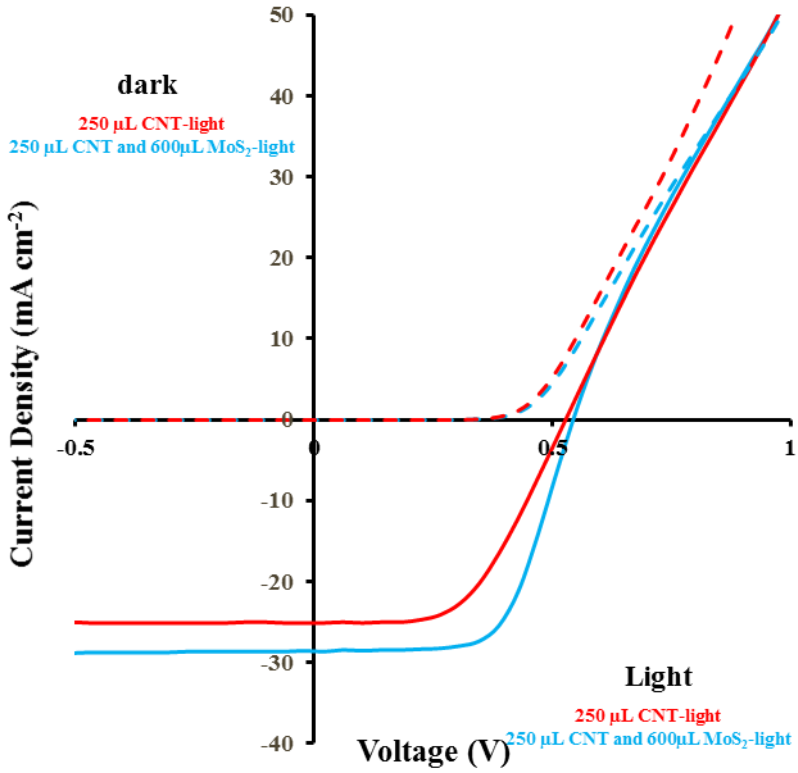

Figure 24: *(J-V) curve for best performing cells for Hybrid MoS_2/ SWCNTs-n-Si- solar cells after all three chemical treatments.*

Table 3: *Hybrid MoS_2/ SWCNTs-n-Si- solar cells properties for best performing cells for SWCNTs & MoS_2 in bold text, average properties (the errors are estimated by standard deviation from three cells).*

Volumes	FF	J_{sc} (mA cm^{-2})	PCE%
250 µL CNT	**0.53**	**25.17**	**7.04**
	0.49±0.05	25.4 ±1	6.6±0.4
250 µL CNT /600µL MoS_2	**0.63**	**28.53**	**9.84**
	0.6±0.7	28.7±1.5	9.2±0.7

Figure 25 displays solar cells properties (J_{sc} (mA cm^{-2}), V_{oc} (V), PCE %, and FF). The peak shape of PCE, FF, and J_{sc} are similar. The PCE% of these particular devices with MoS_2 increased range between 7.3 to 9.8% when compared with a PCE% with only CNT which gave 6.6%. Also, FF showed increase upon adding MoS_2 in solar cells due to their ability to extract the hole. There is a slight change in V_{oc} by 0.04 V. J_{sc} appeared fluctuating peak when comparing with only CNTs. It is clear that improvement of PCE% is due to a combination of high FF and J_{sc}.

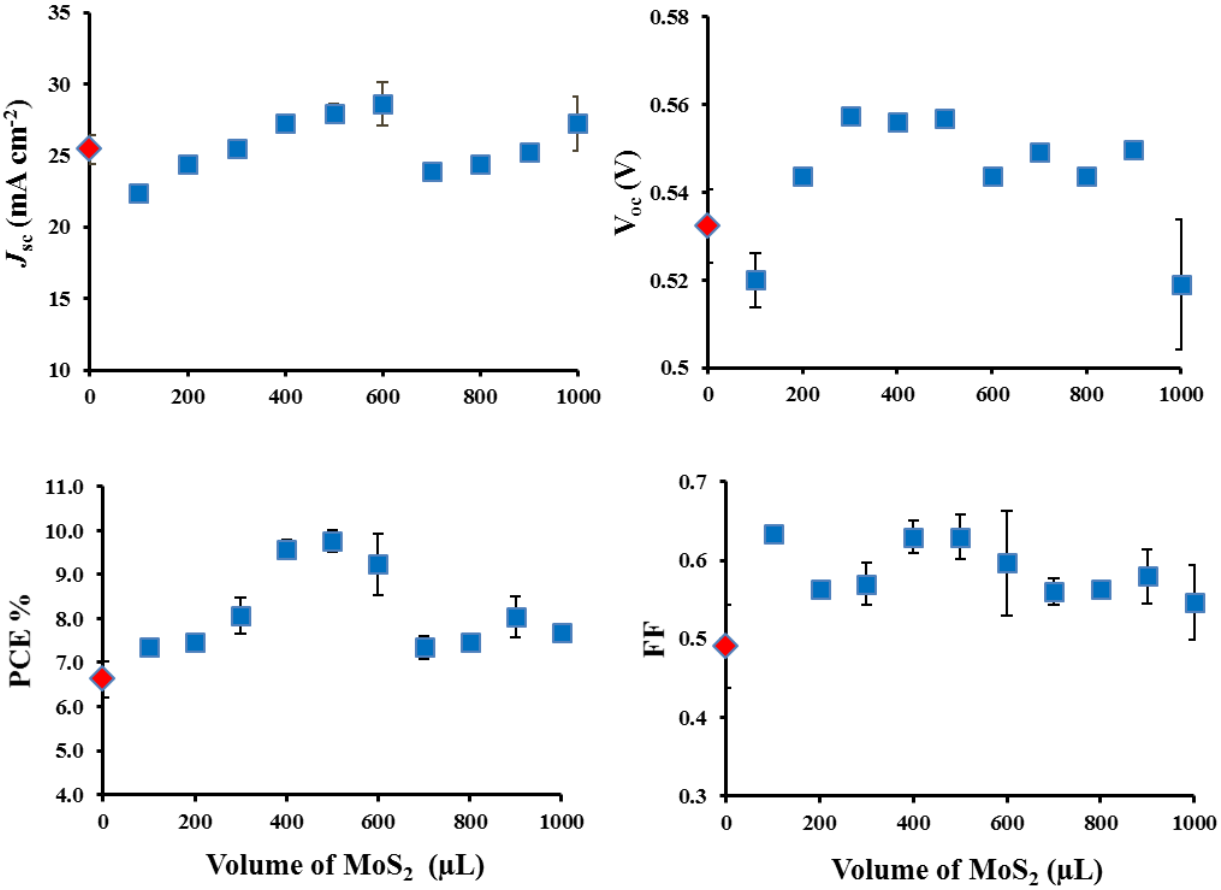

Figure 25: *Hybrid MoS_2/ SWCNTs-n-Si- solar cells parameters extracted after all three chemical treatments.*

3.2.3 Layered SWCNTs @ MoS_2 -n-Si Solar Cells

After building the hybrid devices where the highest efficiency determined was~9.8%, another new device was designed. The design of this experiment was explained in experimental details. In order to know a best thickness of the films that give a best performance, a set of films with different ratio (100-1000µL) of layered MoS_2 and a template of SWCNTs (250µL) was prepared. **Figure26** shows that the transmittance dropped around 10% with increasing amount of MoS_2 and that is expected as adding more material should increase the films

thickness. In addition, sheet resistivity slightly decreased that was expected because of CNTs on the top of the film.\

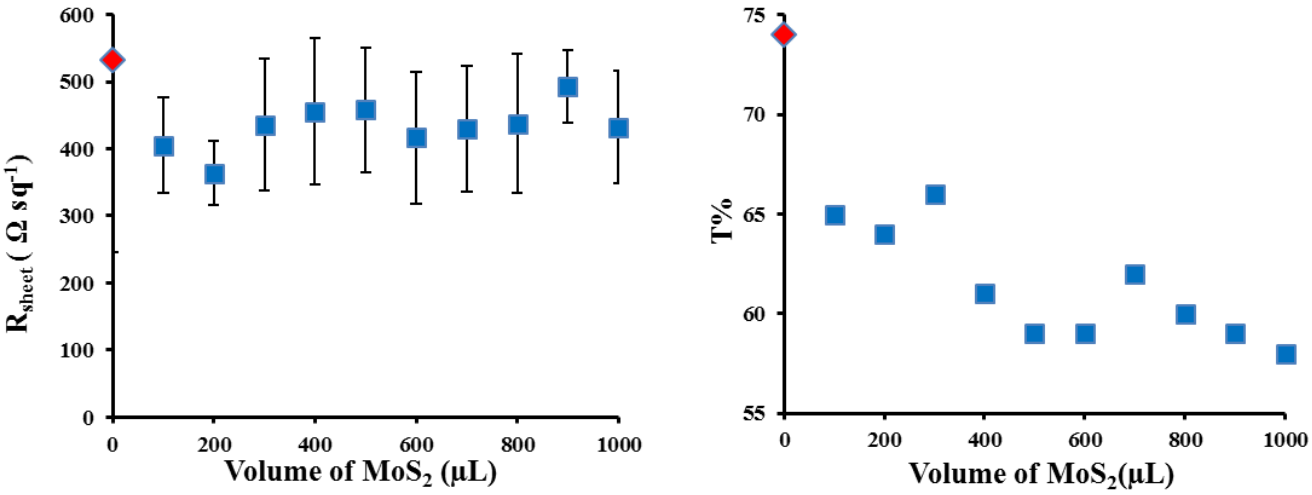

Figure 26: *Transmittance and sheet resistance of layered SWCNTs@ MoS_2 films with various thickness after all three chemical treatments.*

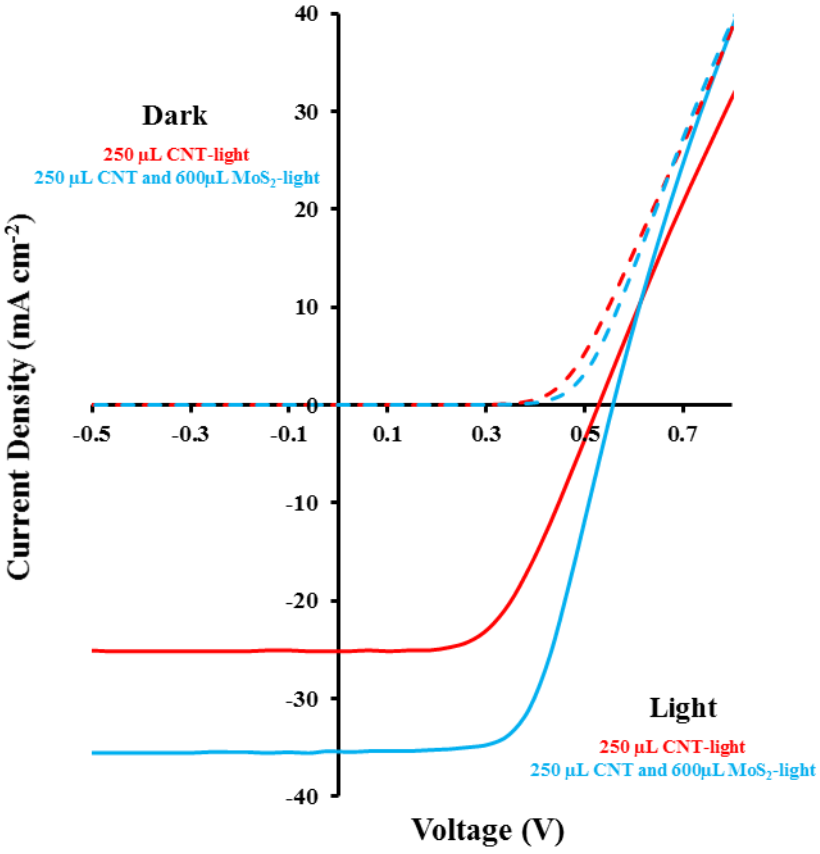

Figure 27: *Current density vs voltage (J/V) curve for best performing cells for layered SWCNTs@ MoS_2-n-Si- Solar cells after all three chemical treatments.*

Table 4: *Layered SWCNTs@ MoS_2-n-Si- Solar cells properties for best performing cells for SWCNTs & MoS_2 in bold text, average properties (the errors are estimated by standard deviation from three cells)*

Volume	FF	J_{sc} (mA cm^{-2})	PCE%
250 µL CNT	**0.53**	**25.17**	**7.04**
	0.49±0.05	25.4 ±1	6.6±0.4
250 µL CNT @600µL MoS_2	**0.61**	**35.46**	**12.04**
	0.6±0.01	32.1±3.1	11.2±0.8

Figure 28 illustrates that J_{sc} and V_{oc} are almost entirely unchanged. The fill factor has been improved by a factor of 40%. Improvement in FFs afford an increase in the highest PCE from 6.7 to 11.2%. **Figure27** and **Table 4** show the best current-density- voltage (J-V) curve of for Layered SWCNTs@ MoS_2-n-Si- Solar cells after all three chemical treatments. The short-circuit current density (J_{sc}) with solar cells that have MoS_2 is highest than the solar has only SWCNTs.

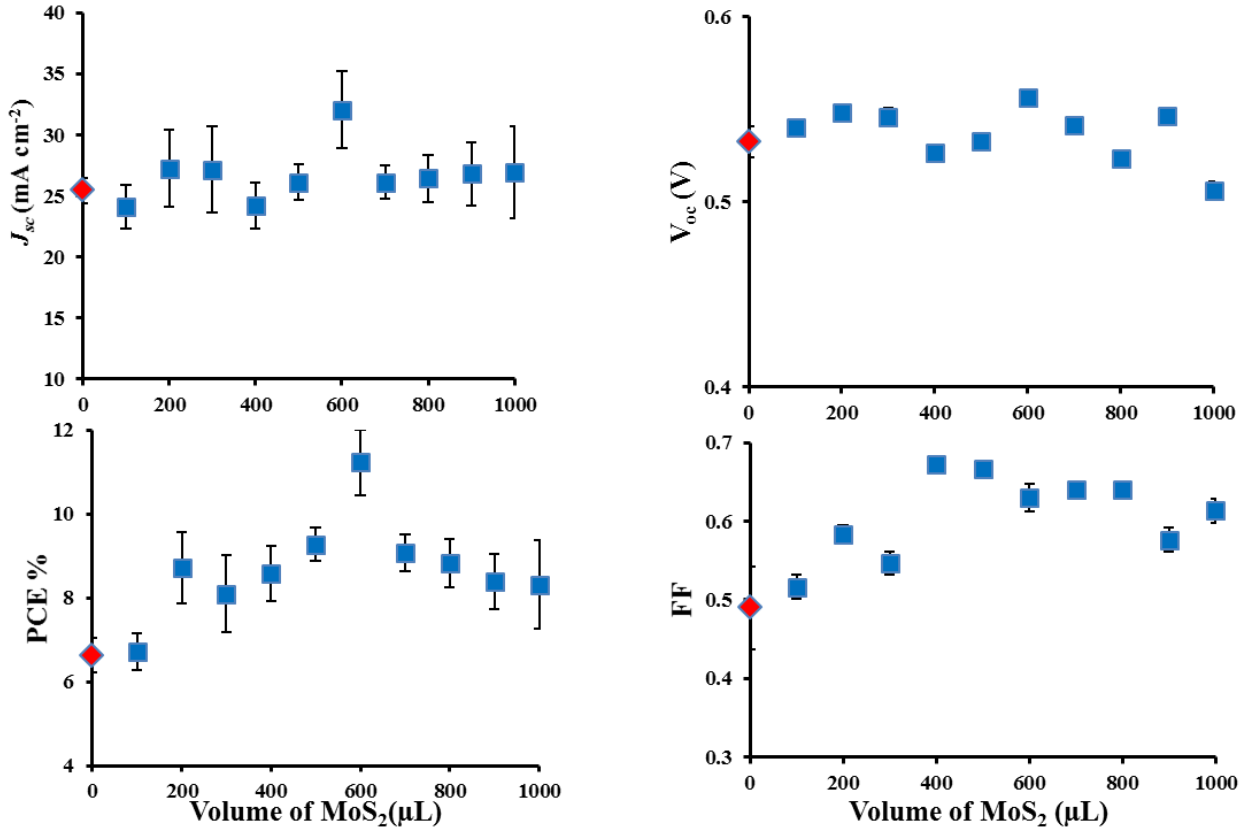

Figure 28: *Layered SWCNTs@ MoS_2-n-Si- Solar cells parameters extracted after all three chemical treatments.*

3.3 comparing hybrid and layered device

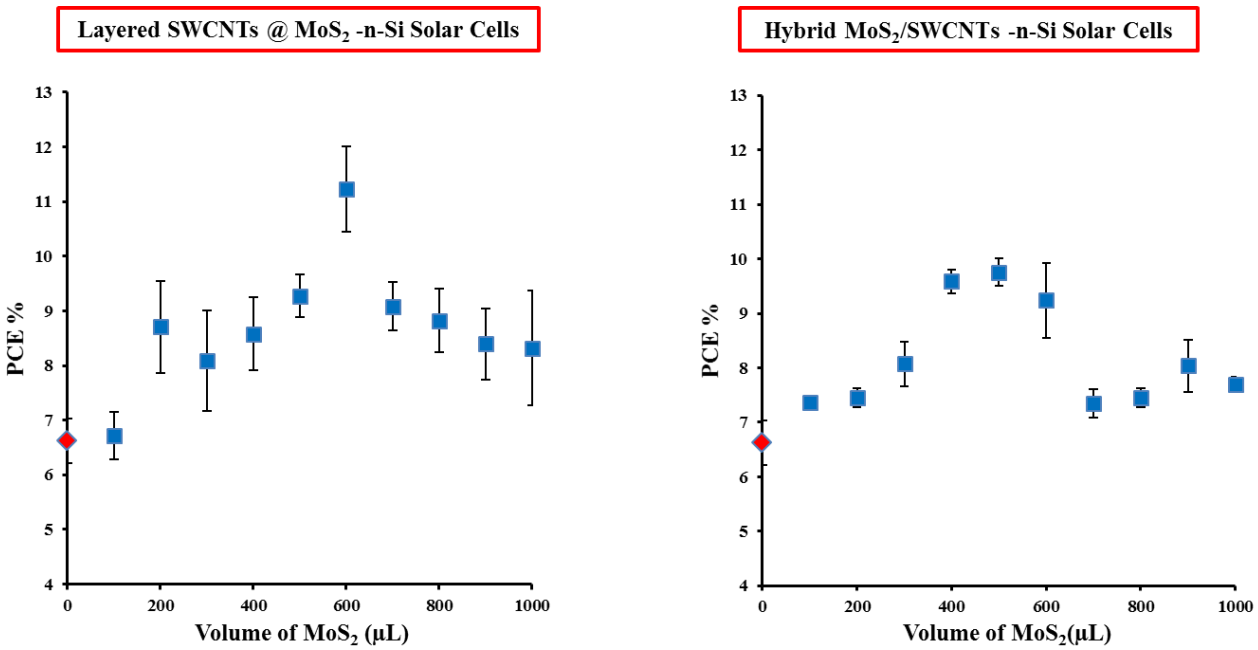

Figure 29: *compering PCE % between layered SWCNTs@ MoS_2-n-Si- Solar cells and hybrid MoS_2/ SWCNTs-n-Si- Solar cells.*

Immediately apparent when comparing layered SWCNTs@ MoS_2-n-Si- Solar cells and hybrid MoS_2/ SWCNTs-n-Si- Solar cells is that PCE % is incresed and improved more in layered MoS_2. The highest values gives ~11.2% as shown in **Figure 29**. Both system of MoS_2 as layered and hybrid have these properties, it has high carrier density that can move lot of charge and the charge can move for long way and there should be another different between them. This result indicates that the value of PCE increases because the layered MoS_2 acts effectivity as a hole extraction layer and help decrease the Schottky barrier height at the interface between the SWCNT films and the Si substrate [19] .

3.4: Energy structure

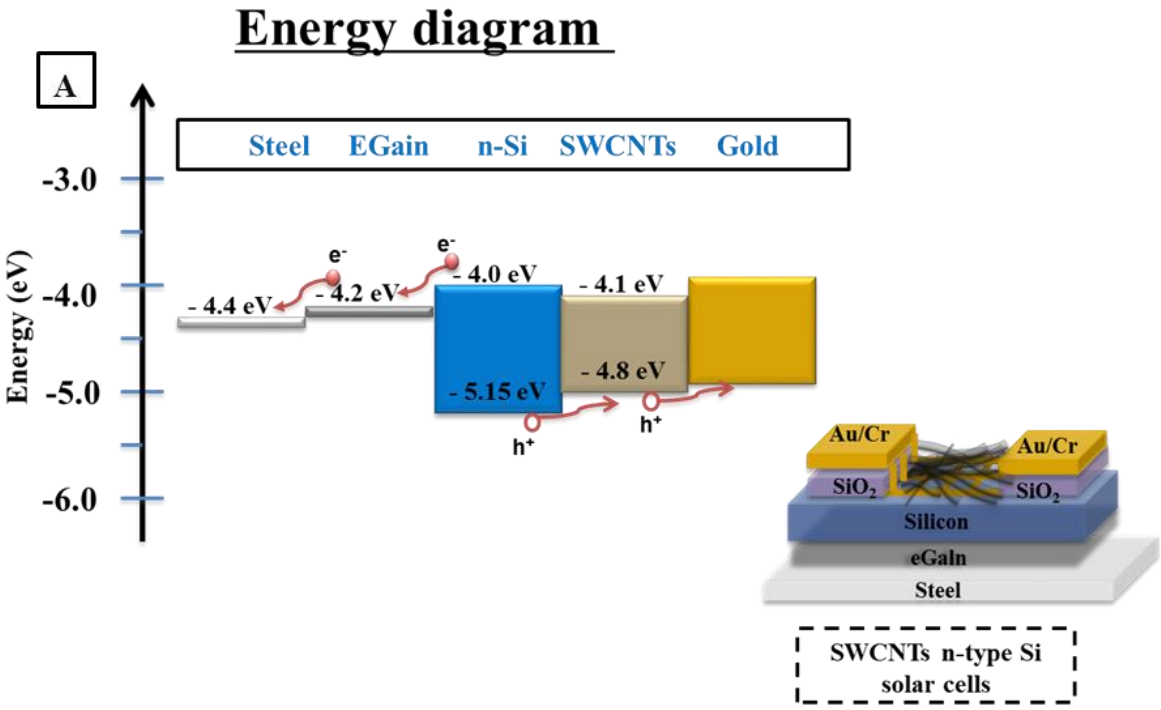

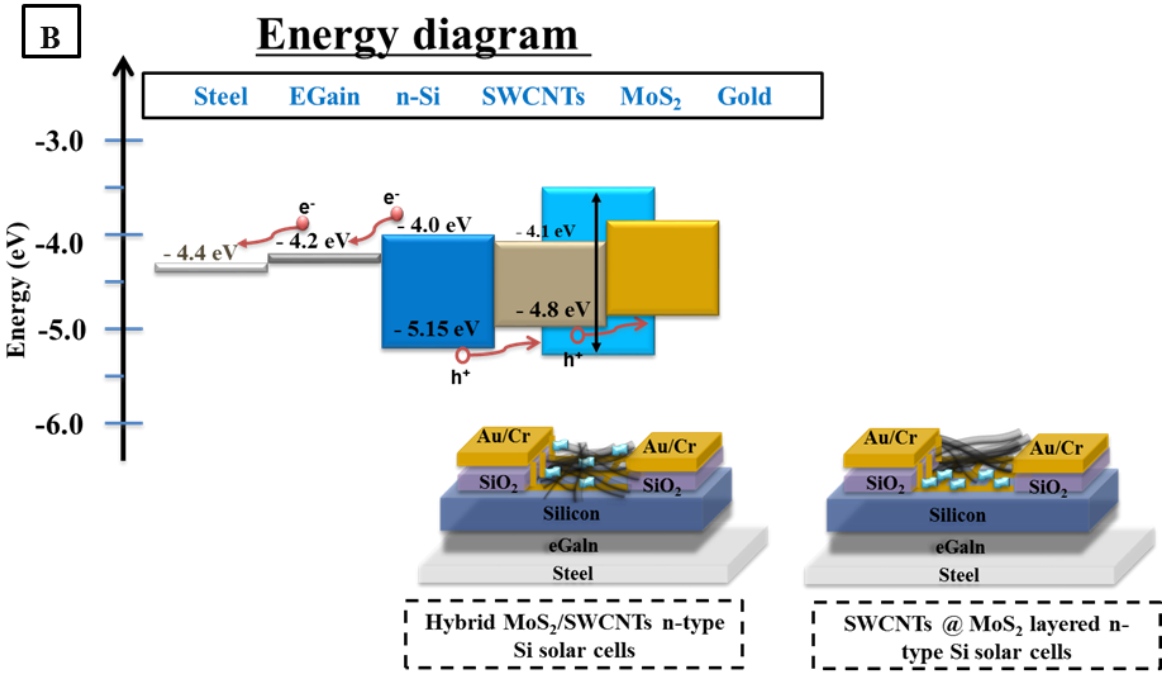

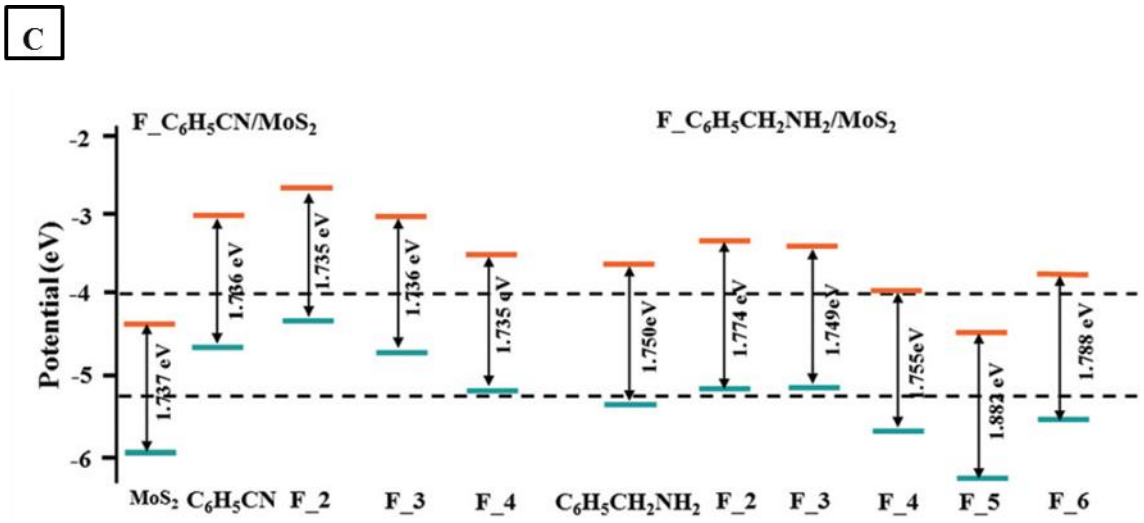

***Figure 30**: Energy diagram (A) for SWCNTs-n-Si- Solar cells, (B) for both layered SWCNTs@ MoS_2-n-Si-Solar cells and hybrid MoS_2/ SWCNTs-n-Si- Solar cells, and (C) studied showing MoS_2 shift when adding with other material* [54].

To have a better understanding of the photovoltaic process, band energy alignment diagrams for the SWCNTs/n-Si and SWCNTs /MoS_2/n-Si solar cells are shown in **Figure 30**. **Figure 30(A)** shows the band diagram of a SWCNTs/n-Si solar cell, where the SWCNTS are p-type. The photovoltaic process in the SWCNTs /n-Si solar cells is understood by the Schottky barrier created at the semiconductor SWCNTs films and (n-Si) substrate. **Figure 30(B)** shows a schematic band alignment for SWCNTs /MoS_2/n-Si solar cells. The exfoliated MoS_2 display n-type properties on the basis of the transport characteristics of the electric double-layer transistor (EDLT). The addition of the MoS_2 layer into SWCNTs /n-Si solar cells changes the band alignment. Indeed, the solar cells properties are enhanced by the addition of the MoS_2 in the layered or hybrid system, as shown in **Figure 29**. The total built-in power conversion efficiency (PCE) of SWCNTs /MoS_2/n-Si solar cells is greater than that of the SWCNTs /n-Si solar cell. The improvement of the built-in field by addition of the MoS_2 can directly increase the FF and the PCE. Furthermore, due to the difference between the Fermi levels, the top of the valence band and the bottom of the conduction band of the MoS_2 at the interface of SWCNTs are shifted. Moreover, in terms of the photogenerated hole, the energy barrier formed by the MoS_2 work as an efficient hole-transfer layer. There is a lot of works showing that MoS_2 energy levels shift up and down depending on how it interacts with others materials[54], so it may be acting as a mediator to help move the holes, as shown in **Figure 30(C)**. The efficient carrier transferring (preventing) layer of MoS_2 efficiently decreases the recombination loss of carriers, which results in an improving of the J_{SC}. Therefore, the MoS_2 as

layered or hybrid between the SWCNTs and n-Si contributes to the improvement of solar cells performance as a carrier-transporting hole.

Chapter 4: Conclusion and Future work

4.1 Conclusion

Molybdenum disulfide (MoS_2) has been successfully used to improve the performance of CNT-Si photovoltaics. Different instruments such as AFM, SEM and Raman were used to characterise MoS_2, SWCNTs and hybrid MoS_2/SWCNTs films in order to examine the thickness and lateral size of MoS_2 and showed the hybrid MoS_2/SWCNTs was mixed well. The MoS_2 nanosheet have thicknesses ranging from 5-90 nm but relatively large lateral dimensions of up to 1µm as observed from the AFM and SEM. Raman spectroscopy showed the presence of MoS_2 and SWCNTs characteristics peaks. Both AFM and Raman techniques confirmed that the MoS_2 was multilayers as compared to literature. Three type of solar cells were designed. The important part was CNT layer in top of Si. Changing of the CNT layer was fabricated by adding MoS_2. The average performance achieved from the CNTs-Si-solar cells only was ~6.6% whereas, the highest PCE after the insertion of MoS_2 to the SWCNTs was 11.2%. Overall, adding the interlayer of molybdenum disulfide has optimised the SWCNTs-n-silicon based solars performance.

4.2 Future work

Producing monolayer or few-layer nanosheets of molybdenum disulfide MoS_2 with large area remains challenging. A scalable, highly efficient and reproducible for approach improve MoS_2 dispersion is critical to decrease the average thickness and increase the average lateral size of flakes. Different techniques, such as determining the time of sonication and the rate of centrifugation method are considered to be the most viable approach [55, 56]. Another method is the electrochemical exfoliation of bulk MoS_2 crystals which can provide monolayer and few-layer of MoS_2 flakes with a large area [57]. Alternatively, using an organic solvent can also potentially achieve this purpose [58] .Therefore, finding a great suspension that has flakes with few layer and bigger lateral dimension would provide a better transporting charge that enhance the efficiency of solar cells.

References

1. Hoffert, M.I., et al., *Energy implications of future stabilization of atmospheric CO2 content.* Nature, 1998. **395**(6705): p. 881.
2. Grace, T., et al., *Use of Carbon Nanotubes in Third-Generation Solar Cells.* Industrial Applications of Carbon Nanotubes, 2016: p. 201.
3. McKinney, M.L. and R.M. Schoch, *Environmental science: Systems and solutions*. 2003: Jones & Bartlett Learning.
4. Agency, U.S.E.P. *Global Greenhouse Gas Emissions Data.* 2017 [cited 2017 31 August]; Available from: https://www.epa.gov/ghgemissions/global-greenhouse-gas-emissions-data.
5. Díaz-González, F., et al., *A review of energy storage technologies for wind power applications.* Renewable and sustainable energy reviews, 2012. **16**(4): p. 2154-2171.
6. Hawkes, A., et al., *Fuel cells for micro-combined heat and power generation.* Energy & Environmental Science, 2009. **2**(7): p. 729-744.
7. Brennan, L. and P. Owende, *Biofuels from microalgae—a review of technologies for production, processing, and extractions of biofuels and co-products.* Renewable and sustainable energy reviews, 2010. **14**(2): p. 557-577.
8. Wenham, S. and M. Green, *Silicon solar cells.* Progress in Photovoltaics: Research and Applications, 1996. **4**(1): p. 3-33.
9. Rinkesh. *What are Alternative Energy Sources?* 2017 [cited 2017 31 August]; Available from: http://www.conserve-energy-future.com/alternativeenergysources.php.
10. Pihl, E., et al., *Material constraints for concentrating solar thermal power.* Energy, 2012. **44**(1): p. 944-954.
11. Jia, Y., et al., *Strong and reversible modulation of carbon nanotube–silicon heterojunction solar cells by an interfacial oxide layer.* Physical Chemistry Chemical Physics, 2012. **14**(23): p. 8391-8396.
12. Bai, X., et al., *Carbon nanotube–silicon hybrid solar cells with hydrogen peroxide doping.* Chemical Physics Letters, 2012. **533**: p. 70-73.
13. Ong, P.-L., W.B. Euler, and I.A. Levitsky, *Hybrid solar cells based on single-walled carbon nanotubes/Si heterojunctions.* Nanotechnology, 2010. **21**(10): p. 105203.
14. Yu, L., et al., *Heterojunction Solar Cells Based on Silicon and Composite Films of Polyaniline and Carbon Nanotubes.* IEEE Journal of Photovoltaics, 2016. **6**(3): p. 688-695.
15. Daniel, D.T. and G.S. Joseph, *Effect of Nanotube Film Thickness on the Performance of Nanotube- Silicon Hybrid Solar Cells.* Nanomaterials, 2013. **3**(4): p. 655-673.
16. Tune, D.D., et al., *Carbon Nanotube-Silicon Solar Cells.* Advanced Energy Materials, 2012. **2**(9): p. 1043-1055.
17. Iijima, S., *Helical microtubules of graphitic carbon.* nature, 1991. **354**(6348): p. 56.
18. Mostofizadeh, A., et al., *Synthesis, properties, and applications of low-dimensional carbon-related nanomaterials.* Journal of nanomaterials, 2011. **2011**: p. 16.
19. Wang, F., et al., *Considerably improved photovoltaic performance of carbon nanotube-based solar cells using metal oxide layers.* Nature communications, 2015. **6**: p. 6305.
20. Yao, Y., et al., *High-Concentration Aqueous Dispersions of MoS_2.* Advanced Functional Materials, 2013. **23**(28): p. 3577-3583.
21. Tsuboi, Y., et al., *Enhanced photovoltaic performances of graphene/ Si solar cells by insertion of a MoS_2 thin film.* Nanoscale, 2015. **7**(34): p. 14476-14482.
22. Mak, K.F., et al., *Atomically thin MoS_2: a new direct-gap semiconductor.* Physical review letters, 2010. **105**(13): p. 136805.
23. Li, X. and H. Zhu, *Two- dimensional MoS_2: Properties, preparation, and applications.* Journal of Materiomics, 2015. **1**(1): p. 33-44.

24. Harper, P. and D. Edmodson, *Electronic band structure of the layer-type crystal MoS_2 (atomic model).* physica status solidi (b), 1971. **44**(1): p. 59-69.
25. Radisavljevic, B., et al., *Single-layer MoS_2 transistors.* Nature nanotechnology, 2011. **6**(3): p. 147-150.
26. Wang, H., et al., *Integrated circuits based on bilayer MoS_2 transistors.* Nano letters, 2012. **12**(9): p. 4674-4680.
27. Li, H., et al., *Fabrication of single-and multilayer MoS_2 film-based field-effect transistors for sensing NO at room temperature.* small, 2012. **8**(1): p. 63-67.
28. Radisavljevic, B., M.B. Whitwick, and A. Kis, *Integrated circuits and logic operations based on single-layer MoS_2.* ACS nano, 2011. **5**(12): p. 9934-9938.
29. Endo, M., S. Iijima, and M.S. Dresselhaus, *Carbon nanotubes*. 2013: Elsevier.
30. Gordon, R., et al., *Structures of exfoliated single layers of WS 2, MoS_2, and MoSe 2 in aqueous suspension.* Physical Review B, 2002. **65**(12): p. 125407.
31. Kappera, R., et al., *Phase-engineered low-resistance contacts for ultrathin MoS_2 transistors.* Nature materials, 2014. **13**(12): p. 1128.
32. Wang, Q.H., et al., *Electronics and optoelectronics of two-dimensional transition metal dichalcogenides.* Nature nanotechnology, 2012. **7**(11): p. 699-712.
33. Eda, G., et al., *Photoluminescence from chemically exfoliated MoS_2.* Nano letters, 2011. **11**(12): p. 5111-5116.
34. Eda, G., et al., *Coherent atomic and electronic heterostructures of single-layer MoS_2.* Acs Nano, 2012. **6**(8): p. 7311-7317.
35. Sun, J., et al., *Synthesis Methods of Two-Dimensional MoS_2: A Brief Review.* Crystals, 2017. **7**(7): p. 198.
36. Grace, T., et al., *Investigating the Effect of Carbon Nanotube Diameter and Wall Number in Carbon Nanotube/Silicon Heterojunction Solar Cells.* 2016.
37. Blanch, A.J., C.E. Lenehan, and J.S. Quinton, *Parametric analysis of sonication and centrifugation variables for dispersion of single walled carbon nanotubes in aqueous solutions of sodium dodecylbenzene sulfonate.* Carbon, 2011. **49**(15): p. 5213-5228.
38. Yu, L., et al., *Optimization of the Metal Front Contact Design for Single-Walled Carbon Nanotube-Silicon Heterojunction Solar Cells.* Solar RRL, 2017. **1**(2).
39. Yu, L., et al., *Application of a hole transporting organic interlayer in graphene oxide/single walled carbon nanotube–silicon heterojunction solar cells.* Journal of Materials Chemistry A, 2017. **5**(18): p. 8624-8634.
40. Gopi, C.V.M., et al., *Carbon nanotube/metal-sulfide composite flexible electrodes for high-performance quantum dot-sensitized solar cells and supercapacitors.* Scientific Reports, 2017. **7**.
41. Aparicio, M.P., et al., *Modeling of photovoltaic cell using free software application for training and design circuit in photovoltaic solar energy*, in *New Developments in Renewable Energy*. 2013, InTech.
42. Goldstein, J., et al., *Scanning electron microscopy and X-ray microanalysis: a text for biologists, materials scientists, and geologists*. 2012: Springer Science & Business Media.
43. Reichelt, R., *Scanning electron microscopy*, in *Science of microscopy*. 2007, Springer. p. 133-272.
44. Bhargava, D.S., *Scanning Electron Microscopy (SEM) lecture* SlideShare, 2016.
45. *Scanning Probe Microscopy Lab (AFM)* KTH Royal Institute of Technology, 2016.
46. Haugstad, G., *Atomic force microscopy: understanding basic modes and advanced applications*. 2012: John Wiley & Sons.
47. Eaton, P. and P. West, *Atomic force microscopy*. 2010: Oxford University Press.
48. Colthup, N., *Introduction to infrared and Raman spectroscopy*. 2012: Elsevier.

49. Dieing, T., O. Hollricher, and J. Toporski, *Confocal raman microscopy*. Vol. 158. 2011: Springer Science & Business Media.
50. *Theory of Raman Scattering.* Bwtek.
51. Dresselhaus, M.S., et al., *Raman spectroscopy of carbon nanotubes.* Physics reports, 2005. **409**(2): p. 47-99.
52. Jamal, G.A. and S. Mominuzzaman, *Different Techniques for Chirality Assignment of Single Wall Carbon Nanotubes.* Journal of Nanoscience and Nanoengineering, 2015. **1**(2): p. 74-83.
53. Liang, L. and V. Meunier, *First-principles Raman spectra of MoS_2, WS 2 and their heterostructures.* Nanoscale, 2014. **6**(10): p. 5394-5401.
54. Pan, J., et al., *Band structure engineering of monolayer MoS_2 by surface ligand functionalization for enhanced photoelectrochemical hydrogen production activity.* Nanoscale, 2014. **6**(22): p. 13565-13571.
55. Coleman, J.N., et al., *Two-dimensional nanosheets produced by liquid exfoliation of layered materials.* Science, 2011. **331**(6017): p. 568-571.
56. Mishra, A.K., K. Lakshmi, and L. Huang, *Eco-friendly synthesis of metal dichalcogenides nanosheets and their environmental remediation potential driven by visible light.* Scientific reports, 2015. **5**: p. 15718.
57. Liu, N., et al., *Large-area atomically thin MoS_2 nanosheets prepared using electrochemical exfoliation.* ACS nano, 2014. **8**(7): p. 6902-6910.
58. Forsberg, V., et al., *Exfoliated MoS_2 in Water without Additives.* PloS one, 2016. **11**(4): p. e0154522.

Appendix

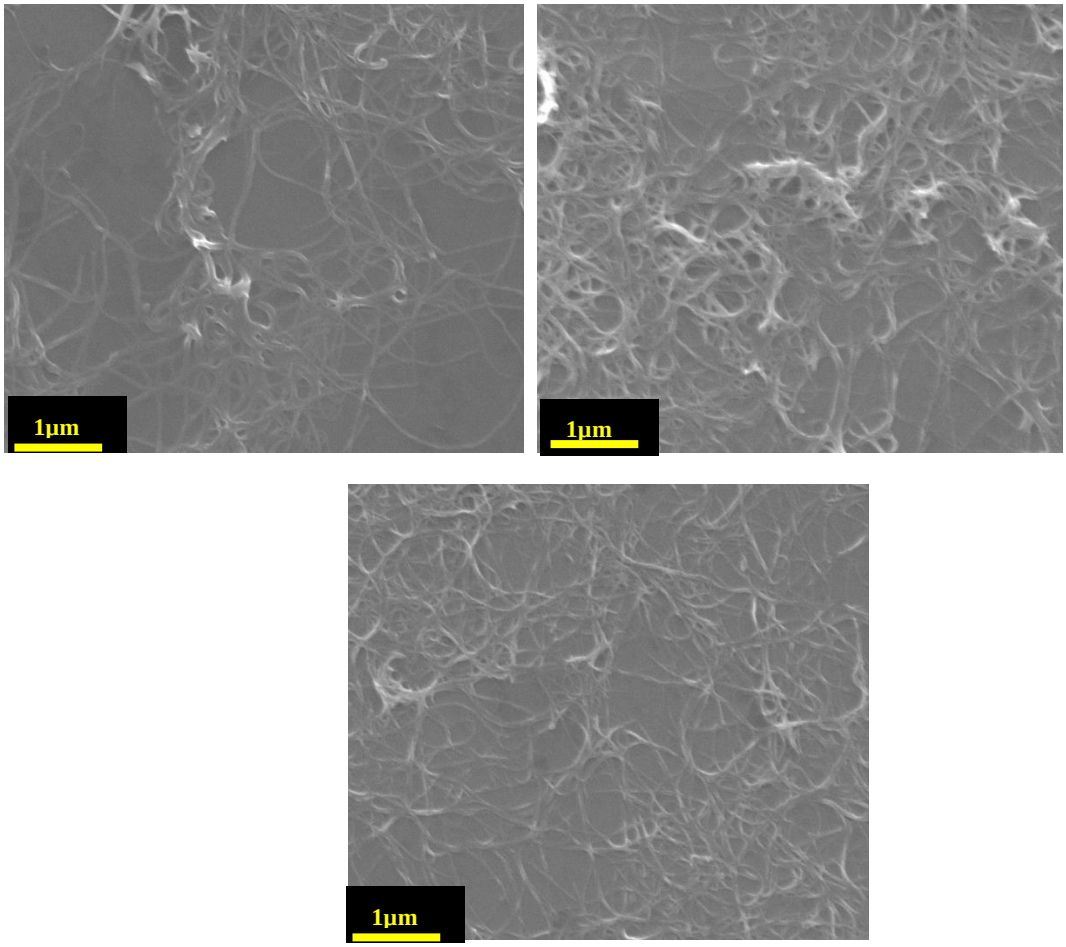

Figure 31: *SEM images of SWCNTs film that deposited on Si substrate*

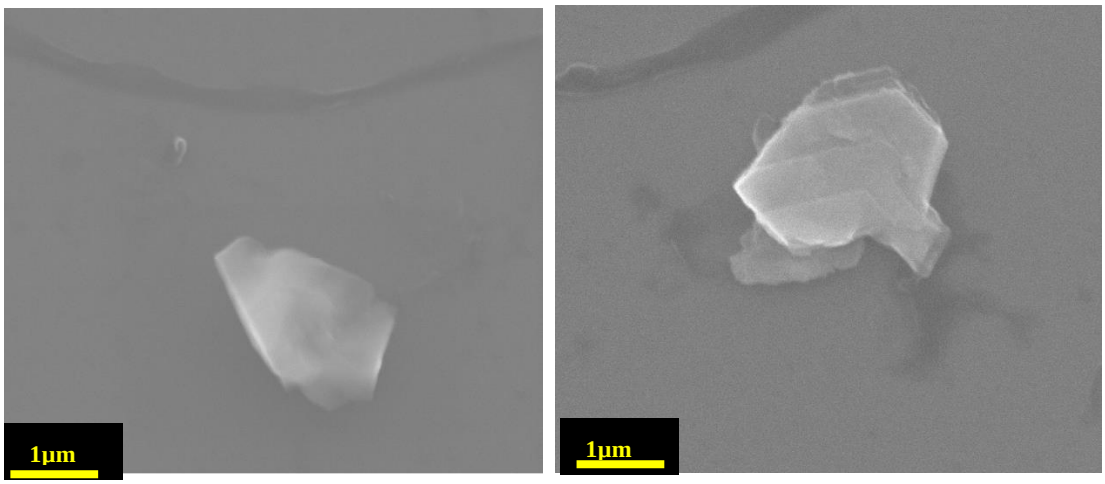

Figure 32: *SEM images of MoS_2 film that deposited on Si substrate*

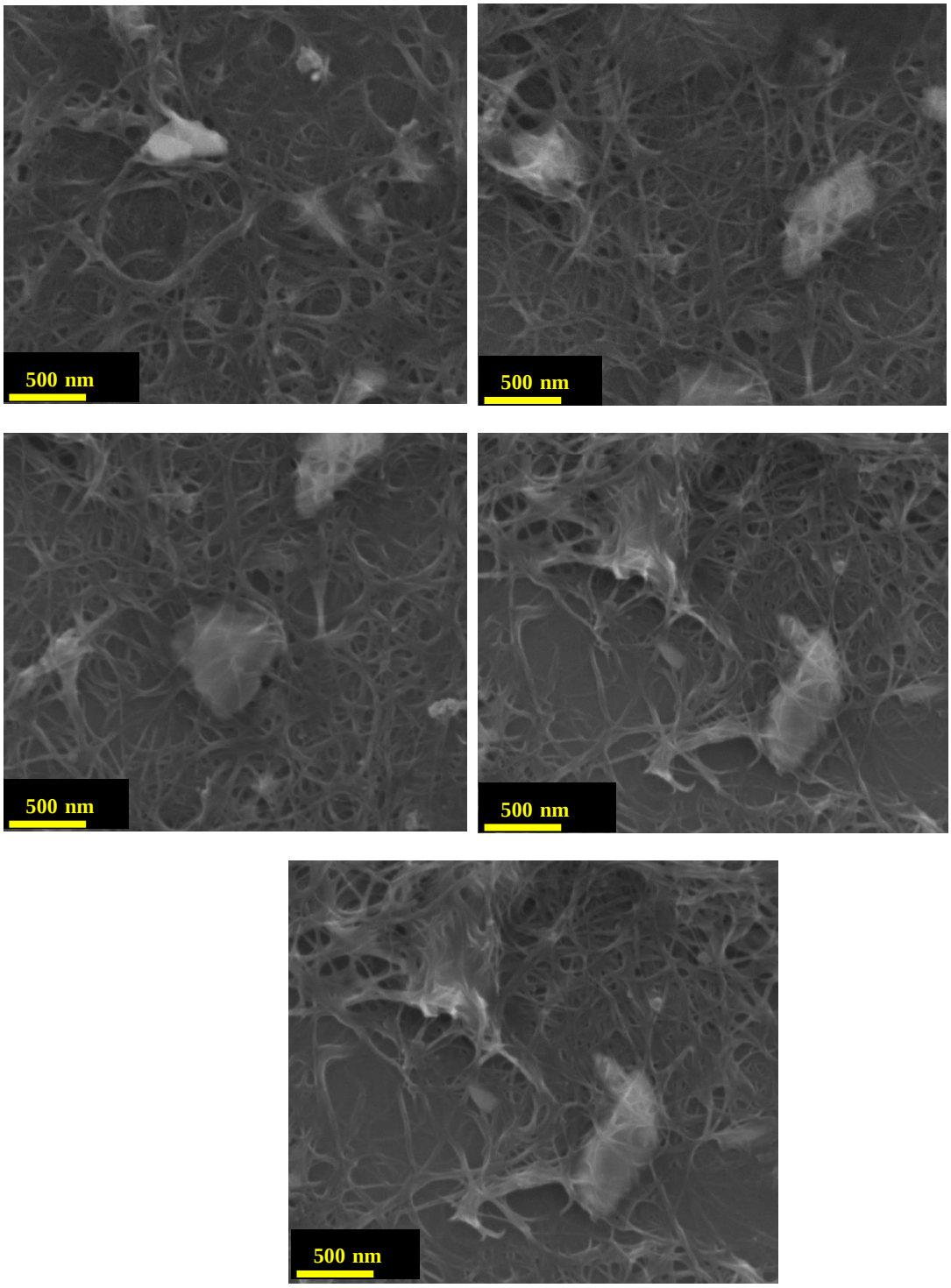

Figure 33: *SEM images of MoS_2 film that deposited on Si substrate*

B

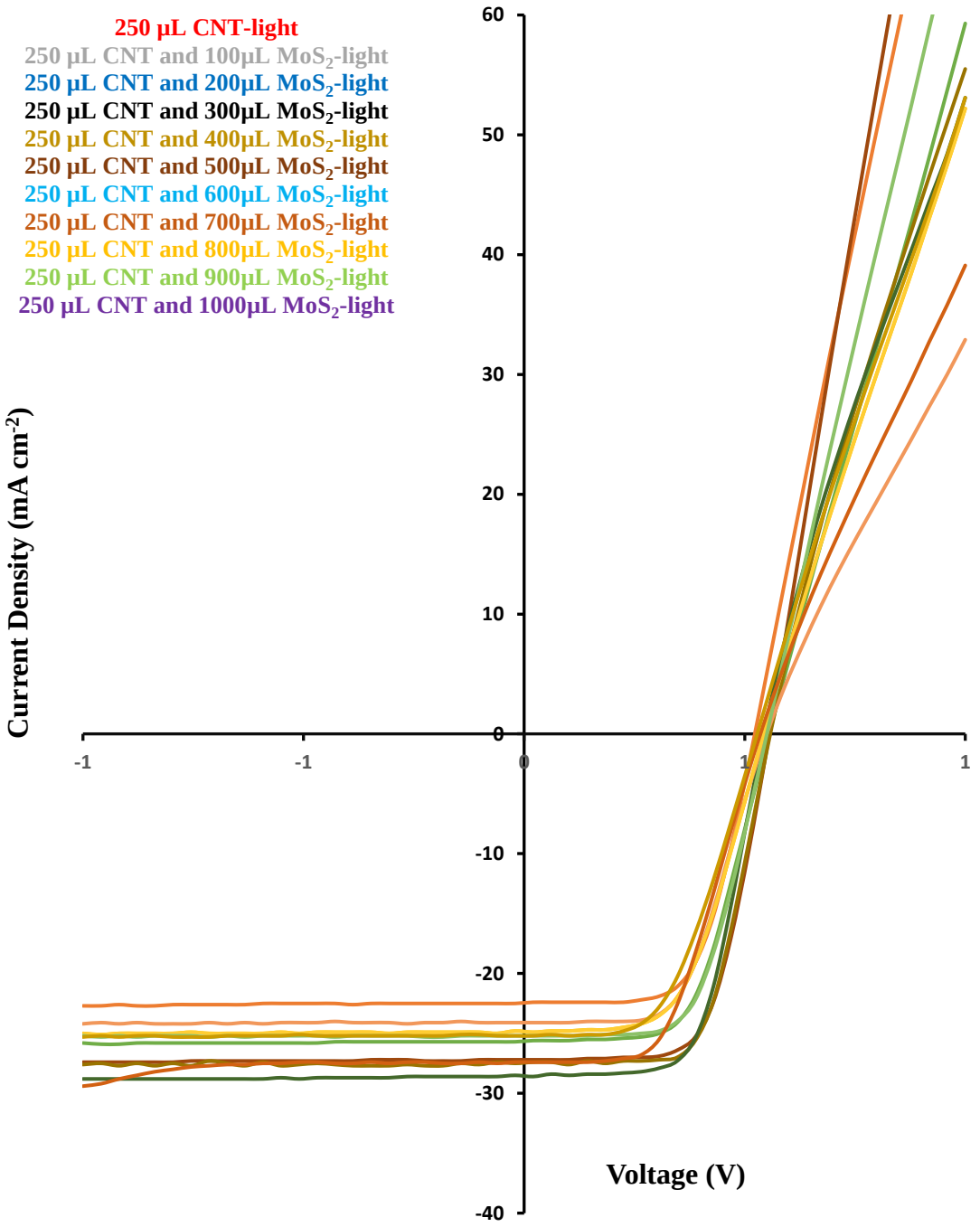

Figure 34: *(J-V) curve for best performing cells for Hybrid MoS_2 (100-1000µL)/ 250µLSWCNTs-n-Si-solar cells after all three chemical treatments.*

TableB1: *Hybrid MoS_2/ SWCNTs-n-Si- solar cells properties for best performing cells*

Volumes	J_{sc} **(mA/cm^{-2})**	V_{oc} **(V)**	**FF**	**Eff (%)**
250 µL CNT-light	25.1	0.52	0.5	7
250 µL CNT and 100µL MoS_2	22.4	0.52	0.6	7.4
250 µL CNT and 200µL MoS_2	24.8	0.54	0.57	7.6
250 µL CNT and 300µL MoS_2	25.6	0.55	0.6	8.5
250 µL CNT and 400µL MoS_2	27.1	0.55	0.65	9.82
250 µL CNT and 500µL MoS_2	27.4	0.5	0.6	9.9
250 µL CNT and 600µL MoS_2	28.5	0.5	0.6	9.8
250 µL CNT and 700µL MoS_2	24	0.55	0.58	7.65
250 µL CNT and 800µL MoS_2	24.8	0.54	0.57	7.64
250 µL CNT and 900µL MoS_2	25	0.55	0.6	8.59
250 µL CNT and 1000µL MoS_2	27.3	0.53	0.53	7.83

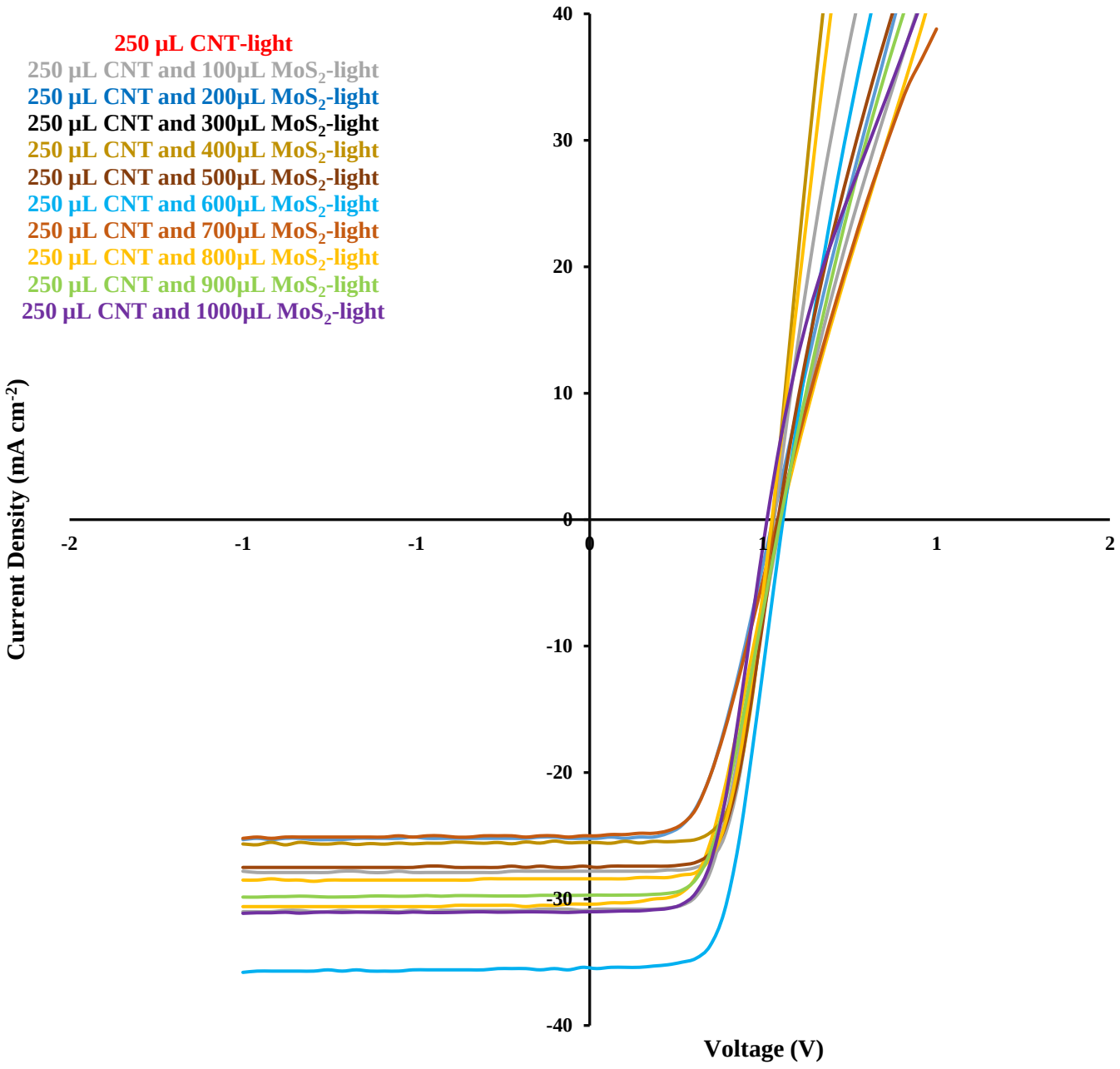

Figure 35: *(J-V) curve for best performing cells for layered MoS_2 (100-1000µL)/ 250µLSWCNTs-n-Si-solar cells after all three chemical treatments.*

TableB2: *Layered MoS_2/ SWCNTs-n-Si- solar cells properties for best performing cells*

Volumes	J_{sc} (mA/cm^{-2})	V_{oc} (V)	FF	Eff (%)
250 µL CNT-light	25.1	0.52	0.5	7
250 µL CNT and 100µL MoS_2	27.8	0.5	0.66	9.72
250 µL CNT and 200µL MoS_2	30.8	0.55	0.57	9.68
250 µL CNT and 300µL MoS_2	30.4	0.55	0.53	8.89
250 µL CNT and 400µL MoS_2	25.5	0.53	0.67	9.11
250 µL CNT and 500µL MoS_2	24.9	0.54	0.52	7.05
250 µL CNT and 600µL MoS_2	35.5	0.55	0.61	12.04
250 µL CNT and 700µL MoS_2	27.4	0.54	0.64	9.51
250 µL CNT and 800µL MoS_2	28.4	0.52	0.63	9.4
250 µL CNT and 900µL MoS_2	29.6	0.55	0.56	9.14
250 µL CNT and 1000µL MoS_2	31	0.51	0.6	9.45